Chapter 15

THEORETICAL AND SIMULATION METHODS APPLIED TO HIGH LATITUDE, F REGION TURBULENCE

J.D. Huba

Space Plasma Branch
Plasma Physics Division
Naval Research Laboratory
Washington, DC 20375-5000

ABSTRACT

A general overview of the theoretical and simulation methods used to study plasma instabilities in the high latitude ionosphere is presented. This is done by way of example, using the $\mathbf{E} \times \mathbf{B}$ instability to illustrate the various techniques. The linear theory is presented from both the fluid and kinetic points of view, as well as both local theory and nonlocal theory. The nonlinear theories of the instability are also discussed, describing both analytical techniques and simulation methods (e.g., pseudo-spectral, finite difference). Finally, we compare the theoretical results with observational data which provides strong evidence that the $\mathbf{E} \times \mathbf{B}$ instability is active in the high latitude F region.

I. INTRODUCTION

The high latitude ionosphere is one of the more exciting regions of the near-earth space environment. This is primarily because it is "connected" to the distant magnetosphere and solar wind, and many phenomena which occur in the high latitude ionosphere are directly related to processes in the magnetosphere and solar wind, perhaps the most spectacular being auroral displays because of their visual impact. In recent years, high latitude plasma turbulence (i.e., electron density irregularities) has received considerable attention in the space plasma physics community [Keskinen and Ossakow, 1983; Kintner and Seyler, 1985; Tsunoda, 1988]. It is known that the scale sizes of plasma irregularities span an enormous range [Kelley et al., 1982; Baker et al., 1983; Rodriquez and Szuszczewicz, 1984], from a few centimeters to thousands of kilometers: eight orders of magnitude! It is clear that a variety of mechanisms are involved in creating this range of structure sizes. The types of mechanisms that have been proposed to explain irregularity production are electron precipitation, plasma mixing by the global convection pattern, plasma and fluid instabilities, etc. Thus, the subject is very interesting, in part, because of its complexity and the interplay of different physical processes. For a recent review of the subject, the interested reader is referred to a recent article by Tsunoda (1988).

There is reasonably good evidence that plasma irregularities with scale sizes $\lesssim$ 10 km are produced primarily by an instability process. Of course, there still remains a large range of scale sizes to be explained. No single instability appears capable of generating all of the observed structure so a number of instabilities have been suggested: $\mathbf{E} \times \mathbf{B}$, Kelvin-Helmholtz, current convective, drift wave, Farley-Buneman, ion cyclotron, ion acoustic, lower hybrid, velocity shear, etc. Within the context of investigating a particular instability and its role in producing ionospheric turbulence, a number of questions should be answered at the outset to clarify the type of analysis to be used and its purpose. What is the equilibrium state of the system? Should fluid theory be used or kinetic theory? Should a local

theory be developed or a nonlocal theory? Should a linear analysis be performed or a nonlinear analysis? What analytical and/or numerical methods are appropriate? The experimental data that one hopes to understand and explain provide the key to answering these questions. It is important to identify the ambient plasma and field conditions, the sources of free energy which can drive a plasma instability, the length and time scales associated with the fluctuations, etc.

The purpose of this paper is to provide an overview of the theoretical and computational methods used to study plasma instabilities in the high latitude ionosphere. We will focus on the $\underline{E} \times \underline{B}$ instability to illustrate the various techniques; this instability is also known as the gradient drift instability and the $\underline{E} \times \underline{B}$ gradient drift instability. The reasons for choosing this instability are as follows. First, the instability is relatively simple to understand and to model. Second, virtually all of the methods available to study a plasma instability have been applied to the $\underline{E} \times \underline{B}$ instability (to my knowledge, the only notable exception are particle and hybrid code simulations). And finally, there is good observational evidence that this instability is one of the causes of plasma structure in the high latitude ionosphere for scale sizes 100's m to 10's km. We add that this paper is very similar to a recent article by Huba (1989), but that we have expanded the analysis in this paper to include ion inertia effects and magnetospheric coupling.

The organization of the paper is as follows. In the next section we present a brief discussion of the ambient plasma and field conditions in the high latitude ionosphere, and provide a physical setting for the instability. In Section III we describe the linear theory of the instability. We present both the fluid theory and the kinetic theory, as well as both the local theory and the nonlocal theory. In Section IV we describe the nonlinear theory of the instability, emphasizing different analytical and numerical methods that have been developed. In Section V we present a discussion of the observational evidence for the $\underline{E} \times \underline{B}$ instability in the high latitude ionosphere, and compare the data with recent simulation results. In Section VI, we summarize the major points of the paper in the final section. We include an Appendix which describes an instability model which incorporates magnetospheric coupling.

II. PHYSICAL MODEL AND EQUILIBRIUM

It is important to first get some feeling for the physical parameters of the high latitude ionosphere, and how they relate to fundamental plasma parameters. In Table I we present typical values for various parameters. In general, one can characterize the high latitude F region as being a weakly collisional, low β, cold plasma.

In Fig. 1 we specify a physical situation which can occur in the high latitude F region and which can lead to the $\underline{E} \times \underline{B}$ instability [Rino et al., 1978; Vickrey et al., 1980]. We show F region "blob": this is a region of enhanced electron density (a factor of 2-10 above ambient) in the altitude regime 200-600 km with a longitudinal extent of ~ 100's km and a latitudinal extent of 1000's km. We also include an eastward ambient electric field $\underline{E}_0$ and note that there is a poleward density gradient on the equator side of the blob.

In Fig. 2 we simplify the physical model in Fig. 1 using a slab coordinate system. We take the ambient magnetic field to be in the z-direction ($\underline{B} = B_0 \underline{e}_z$), the ambient electric field to be in the y-direction ($\underline{E} = E_0 \underline{e}_y$), and the density to be inhomogeneous in the x-direction ($n_0 = n_0(x)$).

The basic equations describing the plasma are the following:

Table I: Typical F Region Parameters

Electron density:	$n_e \approx 10^3 - 10^6$ cm^{-3}
Neutral density:	$n_n \lesssim 10^{12}$ cm^{-3}
Temperature:	$T_e \sim T_i \lesssim 0.1$ ev
Magnetic field:	$B_0 \approx 0.3$ G
Oxygen plasma:	$m_i = 16\ m_p$
Debye length:	$\lambda_{De} \approx 2.7$ mm
Electron gyroradius:	$\rho_e \approx 2.5$ cm
Ion gyroradius:	$\rho_i \approx 4.3$ m
Electron plasma frequency:	$\omega_{pe} \lesssim 5.6 \times 10^7$ sec^{-1}
Electron cyclotron frequency:	$\Omega_e \approx 5.3 \times 10^6$ sec^{-1}
Electron collision frequency:	$\nu_e \lesssim 1.4 \times 10^3$ sec^{-1}
Ion plasma frequency:	$\omega_{pi} \lesssim 3.3 \times 10^5$ sec^{-1}
Ion cyclotron frequency:	$\Omega_i \approx 1.8 \times 10^2$ sec^{-1}
Ion collision frequency:	$\nu_i \lesssim 7$ sec^{-1}
Plasma beta (β):	$\beta \lesssim 4.5 \times 10^{-5}$

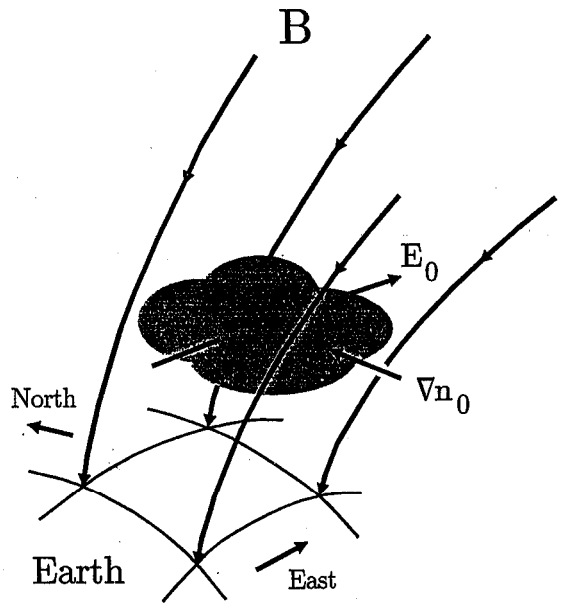

Fig. 1) Schematic showing a high latitude plasma blob. The ambient electric and magnetic fields, and density gradient are oriented so that the $\underline{E} \times \underline{B}$ instability can be excited.

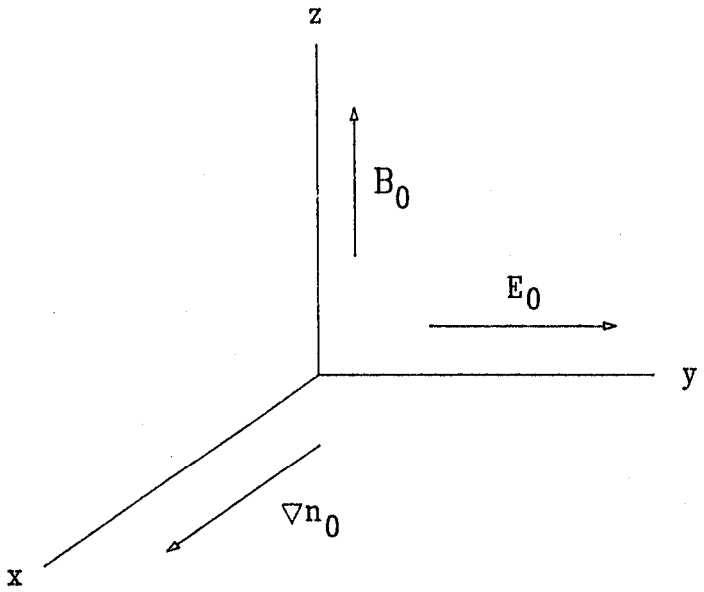

Fig. 2) Slab geometry and plasma configuration used in the analysis.

$$\frac{\partial n_\alpha}{\partial t} + \nabla \cdot n \underset{\sim}{V}_\alpha = 0 \tag{1}$$

$$\frac{d\underset{\sim}{V}_\alpha}{dt} = \frac{e_\alpha}{m_\alpha}\left(\underset{\sim}{E} + \frac{1}{c}\underset{\sim}{V}_\alpha \times \underset{\sim}{B}\right) - \nu_{\alpha n}V_\alpha \tag{2}$$

$$\nabla \cdot \underset{\sim}{J} = 0 \tag{3}$$

where α denotes species (i: ions, e: electrons) and the symbols have their usual meaning. In (2) $\nu_{\alpha n}$ is the particle-neutral collision frequency, we are in the neutral wind frame of reference (i.e., $\underset{\sim}{V}_n = 0$), and we have taken $T = 0$ for simplicity.

The equilibrium drifts are obtained from (2) by setting $d/dt = 0$ and solving for $V_{\alpha 0}$. We obtain

$$\underset{\sim}{V}_{\alpha 0} = \frac{cE_0}{B_0}\hat{e}_x + \frac{\nu_{\alpha n}}{\Omega_\alpha}\frac{cE_0}{B_0}\hat{e}_y \tag{4}$$

The first term in (4) is the usual E x B drift while the second term is the Pedersen drift. Note that the Pedersen drift, unlike the E x B drift, is specie dependent so that it gives rise to the Pedersen current. This current is the source of free energy which drives the $\underset{\sim}{E} \times \underset{\sim}{B}$ instability.

The equilibrium density is obtained from (1) by setting $\partial/\partial t = 0$. Thus, we require

$$\nabla \cdot n_{\alpha 0}(x)\ \underset{\sim}{V}_{\alpha 0} = 0 \tag{5}$$

which leads to $n_{\alpha 0}(x)V_{\alpha 0x} = \text{constant}$. We choose to work in the $\underset{\sim}{E} \times \underset{\sim}{B}$ frame of reference, (i.e., $V'_{\alpha 0x} = V_{\alpha 0x} - cE_0/B_0$) so that $V'_{\alpha 0x} = 0$. Thus, the equilibrium density $n_{\alpha 0}(x)$ can be an arbitrary function of x.

III. LINEAR THEORY

A. Physical Picture

A simple picture of the physical processes involved in the $\underset{\sim}{E} \times \underset{\sim}{B}$ instability is illustrated in Fig. 3. We use the same geometry shown in Fig. 2 but are looking along the z-axis. In Fig. 3 we imagine a "heavy" fluid on top of a "light" fluid; the boundary between these two regions is denoted by the horizontal line. We perturb this boundary with a sinusoidal perturbation. In the F-region the ion Pedersen drift is much larger than the electron Pedersen drift because $\nu_{in}/\Omega_i \gg \nu_{en}/\Omega_e$. Thus, the ions (denoted by the solid line in Fig. 3) drift in the direction of $\underset{\sim}{E}_0$ and leave behind the electrons (denoted by the dashed line in Fig. 3). Because of the charge imbalance that results, a perturbed electrostatic field is set up, as shown. The perturbed electric field $\delta\underset{\sim}{E}$ then causes the plasma to drift with a velocity $\delta\underset{\sim}{V} = c\delta E/B\ \hat{e}_x$. For the directions chosen for ∇n_0 and $\underset{\sim}{E}$, the perturbed velocity acts to enhance the density perturbation: the heavy

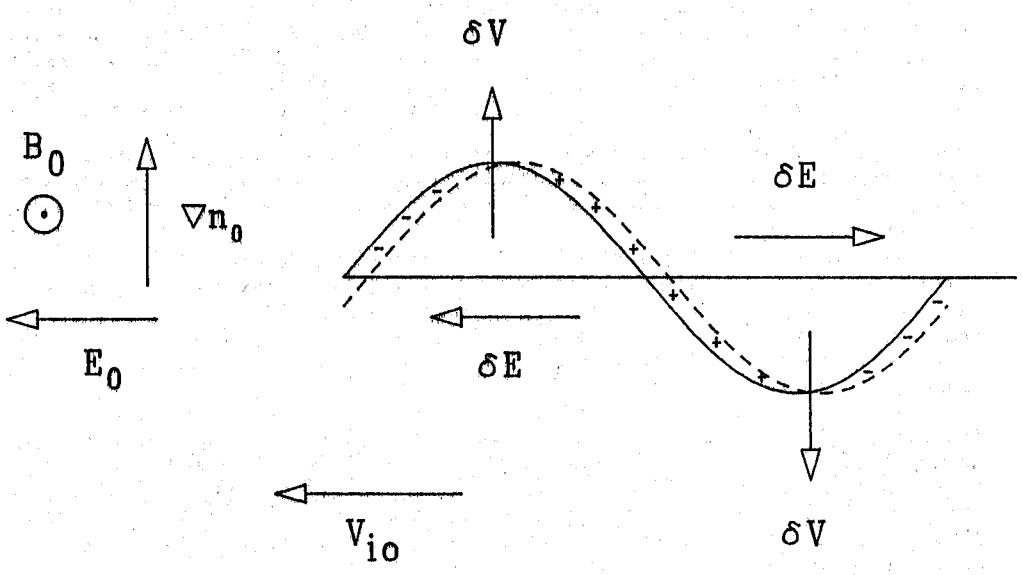

Fig. 3) Schematic showing the physical mechanism of the E x B instability.

fluid falls and the light fluid rises. This is characteristic of an interchange instability, such as the classic Rayleigh-Taylor instability. On the other hand, if the density gradient were chosen in the opposite direction, the perturbation would not grow. Thus, instability will only occur for $\underset{\sim}{E}_0 \times e_z \cdot \nabla n_0 > 0$.

B. Fluid Theory

Fluid theory is a very useful and important method to describe plasma dynamics, e.g., the onset and evolution of plasma instabilities. However, one must always keep in mind the limitations of fluid theory and not apply it to plasma regimes where it is not valid. In general, fluid theory is an appropriate theory to describe a plasma species α when kinetic effects are not important, e.g., in the absence of wave-particle interactions ($\omega \sim kv_\alpha$), finite Larmor radius effects ($kr_{L\alpha} \sim 1$) where v_α is the thermal velocity and $r_{L\alpha}$ is the gyroradius of species α, etc. Thus, one usually assumes the cold plasma, long wavelength approximation ($\omega >> kv_\alpha$ and $kr_{L\alpha} << 1$) when using fluid theory.

With regard to the $\underset{\sim}{E} \times \underset{\sim}{B}$ instability in the ionosphere, fluid theory is valid for $kr_{Li} << 1$ and $\omega << \Omega_i$. This translates into the following spatial and temporal time scales: $\lambda >> 25$ m and $\tau >> 5 \times 10^{-3}$ sec. We note that the instability is a flute mode (i.e., $\underset{\sim}{k} \cdot \underset{\sim}{B}_0 = 0$); there are no wave-particle resonances transverse to B when $\omega << \Omega_i$ (more specifically, $\gamma < \Omega_i$ where γ is the growth rate).

We now derive a dispersion equation which describes the $\underset{\sim}{E} \times \underset{\sim}{B}$ instability in the fluid limit. For simplicity, we make the following assumptions: $kr_{Li} << 1$ (long wavelength), $\omega << \Omega_i$ (low frequency), $n_e \simeq n_i$ (quasi-neutrality), $T = 0$ (cold plasma), $\underset{\sim}{k} \cdot \underset{\sim}{B} = 0$ (flute mode), $\beta << 1$ (low beta), and consider only electrostatic perturbations. In contrast to [Huba, 1989], we include the effects of ion inertia; we allow the ratio ν_{in}/ω to be arbitrary. The basic equations are the following:

$$\frac{\partial n}{\partial t} + \nabla \cdot n \underset{\sim}{V}_e = 0 \tag{6}$$

$$0 = -\frac{e}{m_e}\left(\underset{\sim}{E} + \frac{1}{c}\underset{\sim}{V}_e \times \underset{\sim}{B}_0\right) \tag{7}$$

$$\frac{d\underset{\sim}{V}_i}{dt} = \frac{e}{m_i}\left(\underset{\sim}{E} + \frac{1}{c}\underset{\sim}{V}_i \times \underset{\sim}{B}_0\right) - \nu_{in}\underset{\sim}{V}_i \tag{8}$$

$$\nabla \cdot \underset{\sim}{J} = \nabla \cdot \left[n\left(\underset{\sim}{V}_i - \underset{\sim}{V}_e\right)\right] = 0 \tag{9}$$

We perturb these equations about the equilibrium, i.e., we take $n = n_0(x) + \tilde{n}$, $\underset{\sim}{E} = \underset{\sim}{E}_0 - \nabla\Phi$, and $\underset{\sim}{V}_\alpha = \underset{\sim}{V}_{\alpha 0} + \underset{\sim}{V}_\alpha$ where Φ is the perturbed electrostatic potential. The equilibrium drifts are $\underset{\sim}{V}_{e0} = 0$ and $\underset{\sim}{V}_{i0} = (\nu_{in}/\Omega_i)(cE_0/B_0)e_y$. We take the perturbations to have the following form: $\tilde{p} = \tilde{p}(x)\exp[i(k_y y - \omega t)]$.

Substituting these quantities into (6) - (9) one obtains six equations with six unknowns, ($\tilde{n}$, $\tilde{\phi}$, V_{ex}, V_{ey}, V_{ix}, V_{iy}). After some straightforward algebra these equations can be combined to yield a simple equation for $\tilde{\phi}$:

$$\frac{\partial}{\partial x}\left[n_0 \frac{\partial \tilde{\phi}}{\partial x}\right] - n_0 k_y^2 \left[1 + \frac{\nu_{in}}{\omega} \frac{1}{\omega + i\nu_{in}} \frac{cE_0}{B_0} \frac{n_0'}{n_0}\right]\tilde{\phi} = 0 \qquad (10)$$

where $n_0' = \partial n_0/\partial x$. Interestingly, in the limit of strong collisions (i.e., $\nu_{in} >> \omega$), we note that the mode equation is independent of the ion neutral collision frequency.

(1) Local Theory. In general, one usually solves (10) using the local approximation. This approximation, also referred to as the short wavelength limit, is based on the assumption that $\lambda << L_n$ where λ is the wavelength of the perturbation and L_n $(= (\partial \ln(n_0)/\partial x)^{-1})$ is the density gradient scale length. This is shown schematically in Fig. 4a; the plasma fluctuations are on a much smaller scale than the scale of associated with the change in ambient density.

The advantage of the local approximation is that one assumes that the perturbations are Fourier modes even in the inhomogeneous direction, i.e., $\tilde{p} \propto \exp[i(k_x x + k_y y - i\omega t)]$. If one further assumes that $k_y L_n >> k_x L_n >> 1$ then the first term in (10) can be neglected, and the dispersion equation is simply given by [Ossakow et al., 1978]

$$\omega(\omega + i\nu_{in}) + \nu_{in} \frac{V_0}{L_n} = 0 \qquad (11)$$

where $V_0 = cE_0/B_0$ and $\omega = \omega_r + i\gamma$. We evaluate $1/L_n = n_0'/n_0$ at some $x = x_0$, typically where maximum growth occurs. Equation (11) can be simplified by considering the collisional and inertial limits, i.e., $\nu_{in} >> \omega$ and $\nu_{in} << \omega$, respectively. It is easily shown that

$$\gamma = \begin{cases} V_0/L_n & ; \ \nu_{in} >> \omega \ \text{(collisional)} \\ (V_0/L_n \nu_{in})^{1/2} & ; \ \nu_{in} << \omega \ \text{(inertial)} \end{cases} \qquad (12)$$

From (12) we note that (1) instability only occurs when V_0 and L_n (or E_0 and n_0') are both positive or negative (i.e., in general, $\vec{E}_0 \times \vec{e}_z \cdot \nabla n_0 > 0$), (2) the mode is purely growing (i.e., $\omega_r = 0$), (3) the growth rate is independent of wavenumber k, and (4) the growth rate is largest in the collisional limit.

(2) Nonlocal Theory. The other analytical method for solving (10) is based on nonlocal theory. In this case one assumes $\lambda >> L_n$, i.e., the long wavelength approximation [Huba and Zalesak, 1983; 1984]. This is shown schematically in Fig. 4b. Here, the plasma fluctuation scale length is much longer than the scale associated with the change in ambient density (e.g., surface waves (9)).

For this situation one must solve the differential equation (10). The easiest way is to assume a density profile given by a step function, i.e.,

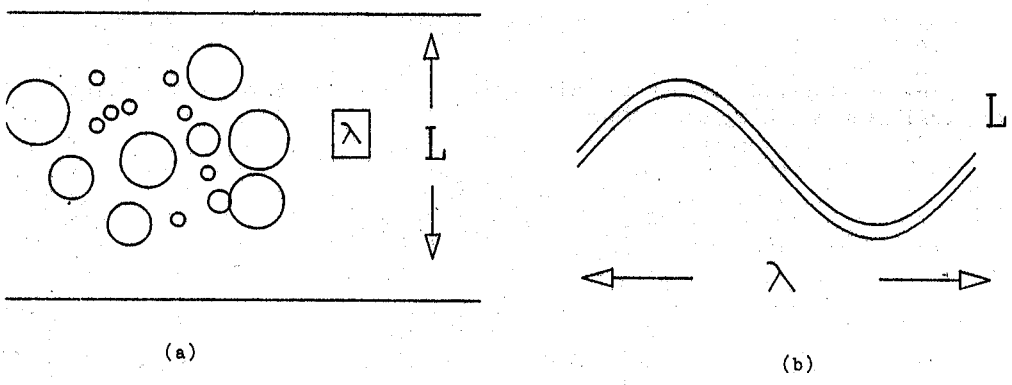

Fig. 4) Schematic showing the distinction between the (a) short wavelength limit and the (b) long wavelength limit.

$$n_0(x) = \begin{cases} n_2 & x > 0 \\ n_1 & x < 0 \end{cases} \tag{13}$$

The perturbed potential is assumed to be

$$\tilde{\phi}(x) = \begin{cases} \phi_2 e^{-k_y x} & x > 0 \\ \phi_1 e^{k_y x} & x < 0 \end{cases} \tag{14}$$

Integrating (10) across the discontinuous density layer at $x = 0$ yields the following matching conditions:

$$n_0 \frac{\partial \tilde{\phi}}{\partial x}\Big|_{-\varepsilon}^{\varepsilon} = - ik_y^2 \frac{cE_0}{B_0} \frac{1}{\omega} n_0 \Big|_{-\varepsilon}^{\varepsilon} \tag{15a}$$

$$\tilde{\phi}\Big|_{-\varepsilon}^{\varepsilon} = 0 \tag{15b}$$

where we let $\varepsilon \to 0$.

The dispersion equation is obtained by substituting (13) and (14) in the jump conditions given by (15). We then obtain the following dispersion equation

$$\omega(\omega + i\nu_{in}) + \nu_{in} k_y V_0 \frac{n_2 - n_1}{n_2 + n_1} = 0 \quad . \tag{16}$$

Note that (16) is similar to (11); one can recover (16) from (11) by making the substitution $1/L_n = k_y(n_2 - n_1)/(n_2 + n_1)$. The growth rate is easily obtained in the collisional and inertial limits, as in local theory case:

$$\gamma = \begin{cases} k_y V_0 \dfrac{n_2 - n_1}{n_2 + n_1} & ; \ \nu_{in} \gg \omega \quad \text{(collisional)} \\ \left[k_y V_0 \nu_{in} \dfrac{n_2 - n_1}{n_2 + n_1} \right]^{1/2} & ; \ \nu_{in} \ll \omega \quad \text{(inertial)} \end{cases} \tag{17}$$

As in local theory, instability only occurs when V_0 and $(n_2 - n_1)$ are both positive or negative, the mode is purely growing, and the collisional growth rate is larger than the inertial growth rate. However, unlike local theory, the growth rate in the long wavelength limit is proportional to k_y in the collisional limit and to $k_y^{1/2}$ in the inertial limit.

(3) General Picture. In the previous two sections we have presented relatively simple techniques to evaluate (10) analytically. These methods are very useful because they permit analytical solutions which are important in understanding the turn-on criteria associated with the instability, quantitative estimates of the growth rate, and how the unstable modes scale with different parameters (e.g., V_0, k_y, L_n, ...). In general, local theory is usually used (at least initially) because it is easy and because, in general, it yields the largest growth rate. On the other hand, it is important to also consider the nonlocal limit because large scale disruptions of plasma are often observed in which $\lambda > L_n$. Furthermore, some modes are only unstable in the nonlocal limit (e.g., the Kelvin-Helmholtz instability driven by sheared velocity flows transverse to B [Chandrasekhar, 1961]; applications to the high latitude ionosphere are given in Kintner and Seyler (1985) and Keskinen et al. (1988)).

Ultimately, if one wishes to determine the growth rate in the regime $\lambda \sim L_n$ one must solve (10) numerically for a specific density profile. We sketch out a typical solution in Fig. 5 for the $\underset{\sim}{E} \times \underset{\sim}{B}$ instability in the collisional limit. The solid line is the analytical solution given by (11) and (15), and the dashed line is the numerical solution. As expected, the numerical solution asymptotes to the appropriate limits. However, for $k_y L_n$ sufficiently large, i.e., very small wavelengths, additional physical effects enter the picture, such as diffusion and finite Larmor radius effects which have not been included in the analysis.

For the sake of completeness, we write down the appropriate momentum transfer equations which include these additional effects. We do not solve them here but simply give references where they have been solved. The electron momentum transfer equation can be written as

$$0 = -\frac{e}{m_e}\left(\underset{\sim}{E} + \frac{1}{c}\underset{\sim}{V}_e \times \underset{\sim}{B}\right) - \nu_{en}\underset{\sim}{V}_e - \nu_{ei}\left(\underset{\sim}{V}_e - \underset{\sim}{V}_i\right) - \frac{\nabla P_e}{nm_e} \qquad (18)$$

where $P_e = nT_e$. The second and third terms are the collisional drags with neutrals and ions, respectively, and the final term is electron pressure. The combination of collisional drag and pressure results in diffusion damping of the $\underset{\sim}{E} \times \underset{\sim}{B}$ instability.

The ion momentum transfer equation can be written as

$$\frac{d\underset{\sim}{V}_i}{dt} = \frac{e}{m_i}\left(\underset{\sim}{E} + \frac{1}{c}\underset{\sim}{V}_i \times \underset{\sim}{B}\right) - \nu_{in}\underset{\sim}{V}_i - \nu_{ie}\left(\underset{\sim}{V}_i - \underset{\sim}{V}_e\right) - \frac{\nabla P_i}{nm_i} - \nabla\cdot\underset{\sim}{\Pi}_i \qquad (19)$$

which is somewhat more complicated than the electron equation. The additional terms here are (1) collisional drag with the electrons, (2) ion pressure and (3) the ion stress tensor $\underset{\sim}{\Pi}_i$. The ion stress tensor includes the effects of ion-ion collisions and finite Larmor radius corrections. In general, all of the additional terms in (18) and (19) lead to damping (or reduced growth) of the $\underset{\sim}{E} \times \underset{\sim}{B}$ instability [Sperling and Glassman, 1985].

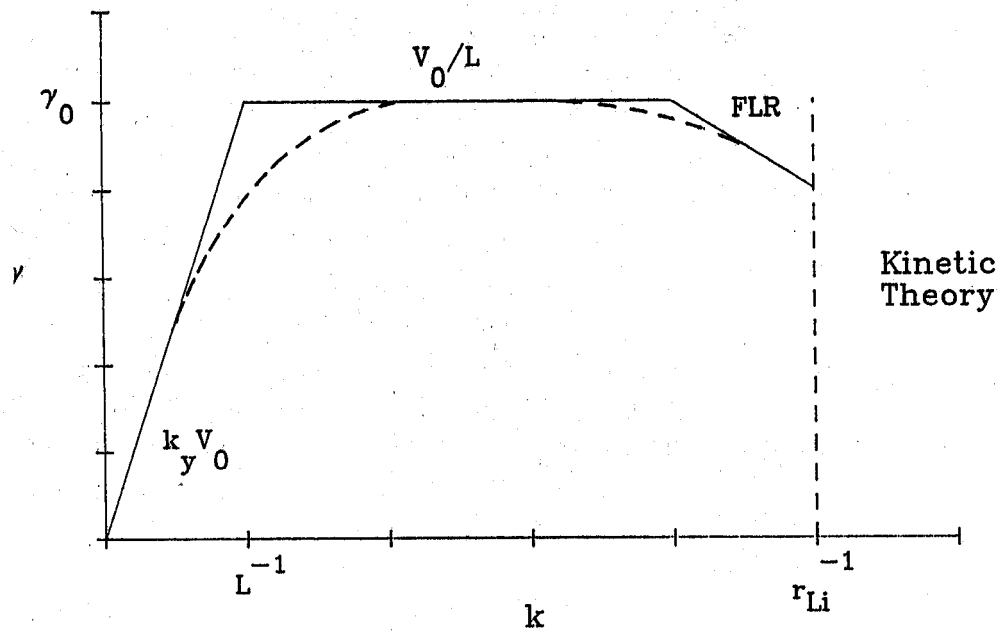

Fig. 5) Sketch of the growth rate (γ) vs wavelength (k) for the $\underline{E} \times \underline{B}$ instability in the fluid limit, i.e., $kr_{Li} < 1$. Kinetic theory is required for the regime $kr_{Li} > 1$ as noted in the figure.

C. Kinetic Theory

As indicated in the previous section, fluid theory has limitations. For the case of the $\underset{\sim}{E} \times \underset{\sim}{B}$ instability, the theory is restricted to the regime $kr_{Li} << 1$. When $kr_{Li} \sim O(1)$ the finite Larmor radius effects become important which cannot be handled by fluid theory. One can use the appropriate ion stress tensor in the fluid limit [Roberts and Taylor, 1962] to gain some understanding of how finite Larmor radius effects influence the instability but one still requires $k_y r_{Li}$ be a small parameter. This is shown schematically in Fig. 5 (labelled FLR). The best (and correct) way to handle the problem is to use kinetic theory: solve the Vlasov equation with an appropriate collision model. This method removes all wavelength and temperature restrictions.

To my knowledge, very little work has been done on the kinetic theory of the $\underset{\sim}{E} \times \underset{\sim}{B}$ instability. This is because observations of plasma structure have focused on the wavelength regimes 100's m - 10's km so that fluid theory is more than adequate. Gary and Cole (1983) have presented a kinetic theory of the $\underset{\sim}{E} \times \underset{\sim}{B}$ instability; however, their formulation is questionable because they did not consider the ion Pedersen drift in the orbit equations. We now outline a kinetic theory of the $\underset{\sim}{E} \times \underset{\sim}{B}$ instability; a detailed analysis can be found in Huba et al. (1989).

The starting point of kinetic theory is the Vlasov equation using the Krook collision model:

$$\frac{\partial f_\alpha}{\partial t} + \underset{\sim}{v} \cdot \frac{\partial f_\alpha}{\partial \underset{\sim}{x}} + \frac{e_\alpha}{m_\alpha}\left[\underset{\sim}{E} + \frac{1}{c}\,\underset{\sim}{v} \times \underset{\sim}{B}\right] \cdot \frac{\partial f_\alpha}{\partial \underset{\sim}{v}} = -\nu_{\alpha n}\left[f_\alpha - \frac{\tilde{n}_\alpha}{n_\alpha} f_\alpha^M\right] \tag{20}$$

where f_α is the distribution function, f_α^M is a Maxwellian distribution function, $\nu_{\alpha n}$ is the collision frequency with neutrals, and $\tilde{n}_\alpha$ is the perturbed density (all of species α).

The first step in solving (20) is to determine the zeroth-order distribution function $f_\alpha^0(x,\chi)$ (i.e., the equilibrium distribution function). The equilibrium distribution function for the electrons and ions can be written as functions of the single-particle constants of motion in the unperturbed fields. For electrons we take

$$F_{e0}(v_\perp^2,\, v_z^2,\, X) = n_0(X)(\pi v_e^2)^{-3/2} \exp[(v_\perp^2 + v_z^2)/v_e^2] \tag{21}$$

where $v_\perp^2 = v_x^2 + (v_y - V_0)^2$, $X = x - (v_y - V_0)/\Omega_e$, $V_0 = cE_0/B_0$, and $v_e = (2T_e/m_e)^{1/2}$. The unperturbed electron distribution function can be expanded locally about some $x = x_0$ based upon the weak inhomogeneity approximation which yields

$$F_{e0}(v_\perp^2,\, v_z^2) \simeq n_0(\pi v_e^2)^{-3/2} \exp[-(v_\perp^2 + v_z^2)/v_e^2]\left(1 - \frac{v_y - V_E}{\Omega_e L_n}\right) \tag{22}$$

where n_0 and L_n are evaluated locally. Note that we are using the local approximation (i.e., $\lambda << L_n$).

We assume a local, drifting Maxwellian distribution for the ions given by

$$F_{i0}(v_\perp^2, v_z^2) = n(\pi v_i^2)^{-3/2}\exp[-(v_\perp^2 + v_z^2)/v_i^2] \tag{23}$$

where $v_\perp^2 = v_x^2 + (v_y - V_{0y})^2$, $v_i = (2T_i/m_i)^{1/2}$, $V_{0y} = V_{di} + V_{pi}$, $V_{di} = v_i^2/\Omega_i L_n$ is the ion diamagnetic drift, and $V_{pi} = (\nu_{in}/\Omega_i)V_0$ is the ion Pedersen drift. The ion diamagnetic drift is proportional to the temperature T_i and was not included in the fluid analysis because we assumed $T_i = 0$.

The next step is to determine the perturbed distribution function f_α. This is usually done by integrating over the unperturbed orbits $x'(\tau)$ (i.e., the method of characteristics, see Krall and Trivelpiece (1973)). For the problem at hand we have

$$\delta f_\alpha = -\frac{e_\alpha}{m_\alpha}\int_{-\infty}^{0} d\tau \exp[i\underset{\sim}{k}\cdot\underset{\sim}{x}'(\tau) - i(\omega + i\nu_{\alpha n})\tau]\ \nabla\delta\phi\cdot\frac{\partial F_{\alpha 0}}{\partial \underset{\sim}{v}'}$$

$$+ \nu_{\alpha n}\frac{\delta n_\alpha}{n}\int_{-\infty}^{0} d\tau \exp[ik\cdot x'(\tau) - i(\omega + i\nu_{\alpha n})\tau]F_{\alpha 0}\ . \tag{24}$$

Finally, after the perturbed distribution function is found, one then calculates the perturbed density fluctuation $\tilde{n}_\alpha = \int d^3v\ f_\alpha$ and substitutes it into Poisson's equation $\nabla^2\tilde{\phi} = 4\pi(\tilde{n}_i - \tilde{n}_e)$ to determine the electrostatic dispersion equation. One finds that the dispersion equation is given by

$$D(\omega,k) = 1 + \chi_e + \chi_i = 0 \tag{25}$$

where

$$\chi_i = \frac{\omega_{pi}^2}{k^2 v_i^2}\left[1 - \frac{(\omega - k_y V_{di} - k_y V_{pi} + i\nu_{in})G_i}{1 - i\nu_{in}G_i}\right]$$

$$\chi_e = \frac{\omega_{pe}^2}{k^2 v_e^2}\left[1 - \frac{(\omega - k_y V_{de} + i\nu_{in})G_e}{1 - i\nu_{en}G_e}\right]$$

and $G_i = \exp(-b_i)I_0(b_i)/(\omega + k_y V_{pi} + i\nu_{in})$, $G_e = \exp(-b_e)I_0(b_e)/(\omega + i\nu_{en})$, $\omega_{p\alpha}^2 = 4\pi ne^2/m_\alpha$, $V_{d\alpha} = v_\alpha^2/\Omega_\alpha L_n$, $V_{pi} = (\nu_{in}/\Omega_\alpha)V_0$, $V_0 = cE_0/B_0$, $b_\alpha = k_y^2 v_\alpha^2/\Omega_\alpha^2$, and I_0 is the modified Bessel function of order 0. In writing χ_α we have assumed flute perturbation ($k\cdot B_0 = 0$), and have taken $\omega/\Omega_\alpha \ll 1$ and $\nu_{\alpha n}/\Omega_\alpha \ll 1$. In the limit $T_e = T_i = 0$ and $\nu_{en} = 0$, one can easily recover (11) from (25).

In Fig. 6 we show the growth rate as a function of kr_{Li} for the following parameters: $V_{di} = 0.01\ v_i$, $V_0 = 0.10\ v_i$, $\nu_{in} = 0.10\ \Omega_i$, $T_i = T_e$, $m_i = 1836\ m_e$, and $\nu_{en} = (0.0,\ 0.1,\ 1.0)\ \Omega_i$. Several interesting features are the following. First, as $kr_{Li} \to 1$ we note that the growth rate decreases in magnitude from its value when $kr_{Li} << 1$ (although it may seem that there is growth when $kr_{Li} = 0$ from Fig. 6, this is not the case as discussed in Section III.B.2). This is a manifestation of finite Larmor radius effects which have a stabilizing influence on the instability. Second, for $\nu_{en} < \nu_{in}$ it is found the growth rate actually maximizes in the regime $kr_{Li} >> 1$. This behavior is analogous to the kinetic interchange mode discussed in Gary and Thomsen (1982). And finally, for $\nu_{en} > \nu_{in}$ one finds that the mode is stable for sufficiently large kr_{Li}. This is caused by electron diffusion damping of the mode, i.e., $\gamma \simeq \gamma_0 - k^2 D$ where $D = \nu_{en} r_{Le}^2$.

IV. NONLINEAR THEORY

Although linear theory is important in determining whether or not an instability can be excited in a specific physical situation (i.e., by providing turn-on criteria and estimates of growth rates), it is only the first step in developing a full understanding of plasma turbulence. The second step, and the more difficult one, involves the development of a nonlinear theory. This is crucial because experimental data are obtained, in general, during the nonlinear (saturated) phase of the instability. Thus, in order to meaningfully compare observational data with theoretical models, a nonlinear theory is clearly needed. For example, predictions of the saturated amplitudes of fluctuating quantities (e.g., $|\tilde{n}|^2$, $|\tilde{E}|^2$) and power spectral densities (e.g., $|\tilde{n}/n_0|^2$ vs k) are useful in making comparisons to the types of data obtained in high latitude experimental campaigns.

As noted above, developing a nonlinear theory is usually much harder than developing a linear theory. Analytical studies are possible and helpful, but usually require a number of simplifying approximations and assumptions in order to make any progress mathematically; unfortunately, these assumptions often break down when applying the theory to realistic ionospheric parameters. To overcome this problem, one can resort to nonlinear numerical simulations which can remove many of the limitations of an analytical theory. However, one must then contend with the subtleties of numerical analysis which is fraught with its own set of difficulties. Nevertheless, large scale computational simulation codes offer the best method to unravel the details of the nonlinear evolution of plasma instabilities.

In this section we will initially discuss analytical techniques used to study the nonlinear evolution of the $\mathbf{E} \times \mathbf{B}$ instability. The emphasis will be on the underlying physics of mode coupling. Following this we will present a discussion of nonlinear simulation studies of the instability.

A. Analytical Results

The major assumptions that are made in developing analytical models of the nonlinear behavior of the $\mathbf{E} \times \mathbf{B}$ instability are the following. First, it is assumed that the fluctuating quantities remain small, i.e., $\tilde{n} << n_0$ and $\tilde{E} << E_0$. Based on this assumption only quadratic nonlinearities are retained. Second, the local approximation is assumed; the perturbation wavelengths are small compared to equilibrium gradient scale lengths (e.g., $\lambda << L_n$ as shown in Fig. 4a). And finally, it is assumed that the density and field fluctuations do not modify the equilibrium. Thus, only

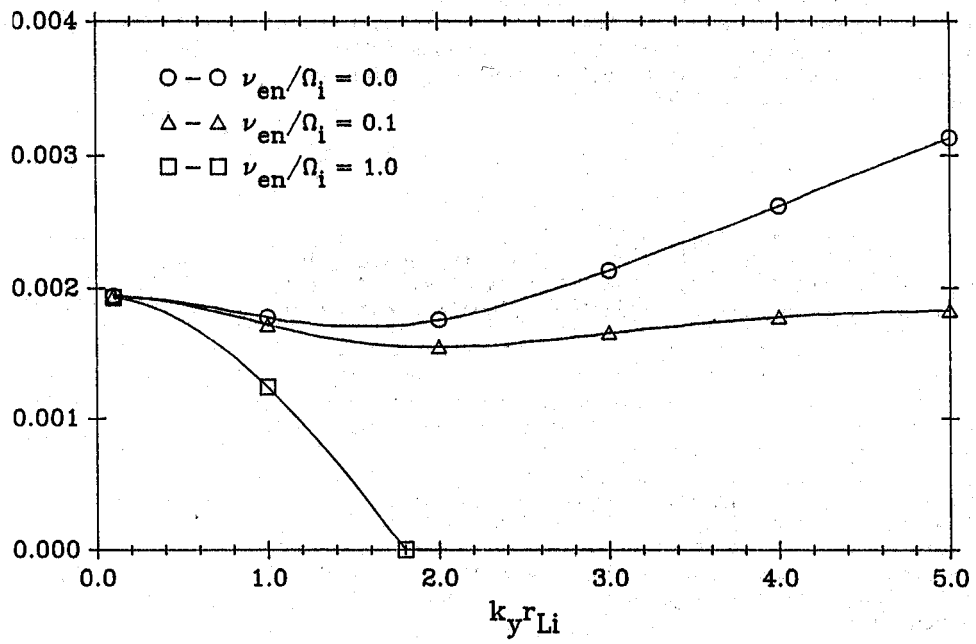

Fig. 6) The growth rate of the $\vec{E}$ x $\vec{B}$ instability (γ/Ω_i) vs wavenumber (kr_{Li}) for different electron collision frequencies. This figure is based upon kinetic (or Vlasov) theory.

perturbations need to be followed in time.

The underlying physical mechanism which saturates the $\underset{\sim}{E} \times \underset{\sim}{B}$ instability in the analyses to be discussed is mode coupling: linearly growing modes couple to linearly damped modes. A steady state is achieved when a balance is reached between the energy being put into growing modes and the energy being removed by some dissipation process. It is crucial that there be an energy sink in this model. Otherwise the instability would grow without bounds because the driver is being held constant. Thus, the equations presented in Section III.B (i.e., (6) - (9)) have to be modified in order to introduce damped modes. This is accomplished by replacing the electron momentum equation (7) with the following equation

$$0 = -\frac{e}{m_e}(\underset{\sim}{E} + \underset{\sim}{V}_e \times \underset{\sim}{B}/c) - \nu_{en}\underset{\sim}{V}_e - \frac{T_e}{m_e}\frac{\nabla n}{n} . \tag{26}$$

As indicated in Section III.B.3, the inclusion of electron-neutral collisional drag and finite electron temperature lead to diffusion damping of the instability. Following the analysis described in Section III, one can easily show that the dispersion equation can be written as

$$(\gamma + \nu_{in})(\gamma + k^2 D) = \frac{k_y^2}{k^2}\frac{\nu_{in} V_0}{L_n} \tag{27}$$

where $k^2 = k_x^2 + k_y^2$ and $D = \nu_{en} r_{Le}^2$ where $r_{Le} = v_e/\Omega_e$ and $v_e = (T_e/m_e)^{1/2}$. The first term in (24) drives the instability; it is similar to (11) but is modified to account for modes with finite k_x. The second term is the damping term; the density fluctuations are "smoothed out" by collisional diffusion. For example, in the collisional limit ($\nu_{in} >> \gamma$), it is easily shown that

$$\gamma = \frac{k_y^2}{k^2}\frac{V_0}{L_n} - k^2 D \tag{28}$$

Given this general background, we now present two examples of theoretical analyses which provide estimates of the saturated amplitudes of the density and field fluctuations, and of the nature of the power spectral density.

(1) Three Mode Coupling. A relatively simple analysis based upon a three mode interaction has been applied to a host of interchange instabilities in the E and F regions (e.g., gradient drift [Rognlien and Weinstock, 1974], collisional Rayleigh-Taylor [Chaturvedi and Ossakow, 1977], $\underset{\sim}{E} \times \underset{\sim}{B}$ [Chaturvedi and Ossakow, 1979], current convective [Chaturvedi and Ossakow, 1981], inertial interchange modes [Huba et al., 1985; Hassam et al., 1986]). This technique provides a simple understanding of the mode coupling process, and an estimate of the saturated fluctuation levels.

The equations used in the analysis are (6), (8), (9), and (26). Perturbing these equations and retaining only quadratic nonlinearities, we arrive at the following set of coupled nonlinear equations for the $\underset{\sim}{E} \times \underset{\sim}{B}$ instability,

$$\frac{\partial}{\partial t}\frac{\tilde{n}}{n_0} - \frac{c}{B}\nabla\tilde{\phi}\times\hat{e}_z\cdot\frac{\nabla n_0}{n_0} - D\nabla^2\frac{\tilde{n}}{n_0} = \frac{c}{Bn_0}\nabla\tilde{\phi}\times\hat{e}_z\cdot\nabla\tilde{n} \tag{29}$$

and

$$\left[\frac{\partial}{\partial t} + \hat{e}_z\times\nabla\tilde{\phi}\cdot\nabla + \nu_{in}\right]\nabla^2\phi = \nu_{in}E_0\,\hat{e}_y\cdot\nabla\frac{\tilde{n}}{n_0} \tag{30}$$

Equation (29) is the electron continuity equation. The second term on the LHS is the linear $\underline{E}\times\underline{B}$ drift, the third term is electron diffusion, and on the RHS is the nonlinear $\underline{E}\times\underline{B}$ drift term which is the only nonlinearity retained. Equation (30) comes from current conservation ($\nabla\cdot\underline{J}=0$) and contains the driver (i.e., the Pedersen drift $\propto V_0$). Linearizing (29) and (30) yields the dispersion equation given by (27).

The nonlinear mode coupling can be seen by substituting the following density and potential fluctuations into (29) and (30): $\tilde{n}\propto\sin(x)\cos(y)$ and $\tilde{\phi}\propto\sin(x)\sin(y)$. It is easily found that the $\underline{E}\times\underline{B}$ nonlinearity in (29) drives a density perturbation $\tilde{n}\propto\sin(2x)$. Thus, we will consider the following perturbations,

$$\tilde{\phi} = \tilde{\phi}_{1,1}\sin(k_x x)\sin(k_y y) \tag{31}$$

$$\tilde{n} = \tilde{n}_{1,1}\sin(k_x x)\cos(k_y y) + \tilde{n}_{2,0}\sin(2k_x x) \tag{32}$$

Substituting (31) and (32) into (29) and (30) yields the following set of mode coupled equations,

$$\frac{\partial\tilde{\phi}_{1,1}}{\partial t} = -\nu_{in}\tilde{\phi}_{1,1} + \nu_{in}E_0\frac{k_y}{k^2}\frac{\tilde{n}_{1,1}}{n_0} \tag{33}$$

$$\frac{\partial\tilde{n}_{1,1}}{\partial t} = -k_y^2 D\,\tilde{n}_{1,1} + \frac{cn_0}{B}\frac{k_y}{L_n}\tilde{\phi}_{1,1} - \frac{c}{Bn_0}k_x k_y\tilde{\phi}_{1,1}\tilde{n}_{2,0} \tag{34}$$

$$\frac{\partial\tilde{n}_{2,0}}{\partial t} = -4k_x^2 D\,\tilde{n}_{2,0} + \frac{c}{B}\frac{1}{2n_0}k_x k_y\tilde{\phi}_{1,1}\tilde{n}_{1,1} \tag{35}$$

The final terms on the RHS of (34) and (35) are the nonlinear coupling terms; note that the coupling leads to damping of the (1,1) mode but to growth of the (2,0) mode. Thus, when the (1,1) mode is linearly unstable (as determined by (27)), it eventually drives the (2,0) mode unstable when the (1,1) mode reaches a sufficiently large amplitude. This in turn causes the growth of the (1,1) mode to slow and eventually stop; ultimately a steady state is achieved. We show a schematic of the mode coupling in Fig.

7. Here, the boundary between growing and damped modes is given by the marginal stability criterion $\gamma = 0$.

We can estimate the saturation levels of the fluctuations by finding the steady state solution to (33) - (35). We let $\partial/\partial t = 0$ and solve for $\tilde{\Phi}_{1,1}$, $\tilde{n}_{1,1}$ and $\tilde{n}_{2,0}$. We find that for a weakly damped system that

$$\tilde{n}_{1,1} = \frac{2k}{k_y} \left(\frac{2D}{V_0 L_n}\right)^{1/2} n_0 \tag{36}$$

$$\tilde{n}_{2,0} = \frac{1}{k_x L_n} n_0 \tag{37}$$

$$\tilde{E}_{1,1} = 2\left(\frac{2D}{V_0 L_n}\right)^{1/2} E_0 \tag{38}$$

where we have taken $\tilde{E}_{1,1} \simeq -k\tilde{\Phi}_{1,1}$ and have assumed $V_0/L_n >> k^2 D$. We can quantify $\tilde{n}$ and $\tilde{E}$ at saturation by using the following high latitude parameters: $V_0 = cE_0/B_0 = 100$ m/sec, $L_n = 10$ km, $k_x = k_y = 0.01$ m^{-1} ($\lambda_x = \lambda_y = 600$ m), $T_e = T_i = 0.1$ ev, $\nu_e = 1000$ sec^{-1}, $r_{Le} = 2.5$ cm, and $D = 1$ m^2/sec. We find that $\tilde{n}_{1,1}/n_0 \simeq 0.4\%$, $\tilde{n}_{2,0}/n_0 \simeq 1.0\%$, and $E_{1,1}/E_0 \simeq 0.3\%$. Thus, the instability can saturate at relatively low levels consistent with the assumption that the fluctuation level be small.

An interesting extension of this analysis has been described in Huba et al. (1985) in which it was demonstrated that the mode coupling equations (33) - (35) reduce to the famous Lorenz equations [Lorenz, 1963]. Thus, this three mode system can exhibit a strange attractor with chaotic behavior. Ion inertia plays a crucial role in this phenomenon in that if it is neglected then the three mode system does not exhibit chaos and a stable convection pattern results.

(2) Power Spectrum. Although the three mode calculation highlights the importance of nonlinear mode coupling and provides estimates of the saturated fluctuation levels, it is a gross simplification of the actual interchange process in the ionosphere because ionospheric turbulence is a many mode phenomenon. Clearly, numerical simulations are needed to follow the complex interaction of large numbers of modes. This will be discussed in the next section. However, an analytic estimate of the spatial power spectrum of the $\underline{E} \times \underline{B}$ instability can be obtained from conservation laws associated with the fundamental plasma fluid equations. As in the three mode system, the analysis is based upon the assumption that a steady state can be achieved via mode coupling; the growing modes are saturated by transferring energy to damped modes. The calculation that follows is from Keskinen and Ossakow (1981) and Keskinen (1989). The interested reader is referred to these articles for more details.

Equations (29) and (30) are the basic equations used in the analysis. We first multiply (29) by $\tilde{n}$ and integrate over all x and y. This leads to the following equation

$$\int dxdy \left[\frac{1}{2}\frac{\partial}{\partial t}|\tilde{n}|^2 - \tilde{n}\nabla\tilde{\phi} \times \hat{e}_z \cdot \nabla n_0 - \tilde{n}\nabla\tilde{\phi} \times \hat{e}_z \cdot \nabla\tilde{n} - D\tilde{n}\nabla^2\tilde{n}\right] = 0 \tag{39}$$

The third term in (39) vanishes upon integration over all x and y because $\tilde{n}$

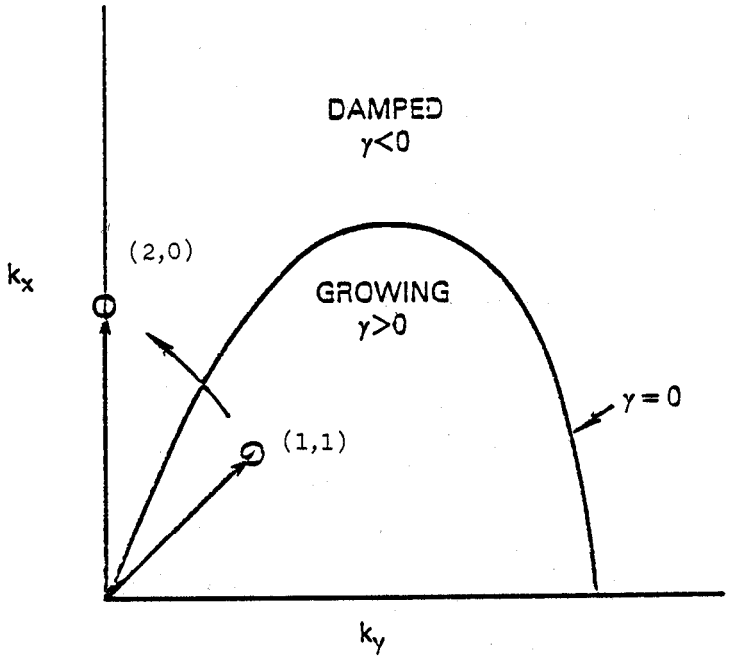

Fig. 7) Schematic showing mode coupling for the $\mathbf{E} \times \mathbf{B}$ instability. The growing and damped modes are shown in $\mathbf{k}$ space. The coupling of the growing (1,1) mode and the damped (2,0) mode is also indicated.

$\to 0$ as $x,y \to \infty$; this can be shown using Gauss' Law. We Fourier expand $\tilde{n}$ and $\tilde{\phi}$ and obtain the following expression from (39)

$$\int dk_x dk_y \left[\frac{1}{2}\frac{\partial}{\partial t} I_{\underset{\sim}{k}} + i\frac{c}{B}\hat{e}_z \times \underset{\sim}{k} \cdot \nabla n_0 \tilde{n}_{-\underset{\sim}{k}} \tilde{\phi}_{\underset{\sim}{k}} + Dk^2 I_{\underset{\sim}{k}}\right] = 0 \tag{40}$$

where $I_{\underset{\sim}{k}} = |\tilde{n}_{\underset{\sim}{k}}|^2$. From (30) we obtain

$$\tilde{\phi}_{\underset{\sim}{k}} = \frac{ik_y E_0}{n_0 k^2} \frac{i\nu_{in}}{\omega + i\nu_{in}} \tilde{n}_{\underset{\sim}{k}} \tag{41}$$

Substituting (41) into (40) we find that

$$\int dk_x dk_y \left[\frac{1}{2}\frac{\partial}{\partial t} I_{\underset{\sim}{k}} - \gamma_{\underset{\sim}{k}} I_{\underset{\sim}{k}}\right] = 0 \tag{42}$$

where

$$\gamma_{\underset{\sim}{k}} \simeq \frac{k_y^2}{k^2}\frac{V_0}{L_n} - k^2 D \qquad ; \nu_{in} >> \gamma \quad \text{(collisional)} \tag{43a}$$

$$\gamma_{\underset{\sim}{k}} \simeq \frac{k_y}{k}\left[\frac{\nu_{in} V_0}{L_n}\right]^{1/2} - \frac{k^2 D}{2} \qquad ; \nu_{in} << \gamma \quad \text{(inertial)} \tag{43b}$$

and we have used (27). Assuming a steady state and transforming to a cylindrical coordinate system, we find from (42) and (43) that

$$\int_{k_{min}}^{k_c} dk\, k \int_0^{2\pi} d\theta\, \gamma^g_{\underset{\sim}{k}} I_{\underset{\sim}{k}} = \int_{k_c}^{k_{max}} dk\, k \int_0^{2\pi} d\theta\, \gamma^d_{\underset{\sim}{k}} I_{\underset{\sim}{k}} \tag{44}$$

where γ_k^g is the positive term in (43) (i.e., the growth term), and γ_k^d is the negative term in (43) (i.e., the damping term). In (43) it is assumed that the waves are linearly unstable in the range $k_{min} - k_c$, and are linearly damped in the range $k_c - k_{max}$; k_c is the wavenumber which corresponds to marginal stability ($\gamma = 0$).

It is now assumed that the spectrum $I(k,\theta)$ has the following form

$$I(k,\theta) = I_0 \cos^m\theta \,(1 + k^2/k_0^2)^{-(n+1)/2} \tag{45}$$

where $m > 0$ and I_0 = constant. Substituting (45) into (44) it can be shown that

$$\left(\frac{k_0}{k_{max}}\right)^{n-1} = \frac{3-n}{n-1} \frac{\Gamma(\frac{m+2}{2})\Gamma(\frac{m+2}{2})}{\Gamma(\frac{m+1}{2})\Gamma(\frac{m+3}{2})} \frac{2(\nu_{in}V_0/L_n)^{1/2}}{k_{max}^2 D} \quad ; \quad \nu_{in} << \gamma \qquad (46a)$$

$$\left(\frac{k_0}{k_{max}}\right)^{n-1} = \frac{3-n}{n-1} \frac{\Gamma(\frac{m+1}{2})\Gamma(\frac{m+4}{2})}{\Gamma(\frac{m+2}{2})\Gamma(\frac{m+3}{2})} \frac{V_0/L_n}{k_{max}^2 D} \quad ; \quad \nu_{in} >> \gamma \qquad (46b)$$

where Γ is the gamma function and is defined as

$$\Gamma(z) = \int_0^\infty dt\ t^{z-1}e^{-t}$$

and it is assumed that $n > 1$ and $k_{min} < k_0 < k_c$. From (46) it is clear that $1 < n < 3$.

For an inverse power law with a spectral index $n = 2$ and $m = 2$ it is found that $k_0 \propto L_n^{-1}$. Equation (46a) is applicable for low altitudes (< 500 km) in the high latitude ionosphere. If we take V_0 = 100 m/sec, $D = 1$ m^2/sec, L_n = 10 km, and $k_{max} = 0.63$ m^{-1} (λ_{min} = 10 m), we find that $2\pi/k_0 \simeq$ 500 m which is consistent with observations [Tsunoda, 1989].

B. Numerical Results

As indicated earlier, large scale numerical simulations offer the best technique to understand the nonlinear evolution of plasma instabilities. In general, two types of simulations have been performed to study the nonlinear evolution of interchange instabilities. One type of simulation focuses on the evolution of small-scale turbulence, i.e., $kL_n >> 1$ (see Fig. 4a). The purpose of these simulations is to obtain an understanding of the cascade of wave energy from large to small wavelengths in two dimensions, and to calculate the spectral characteristics of the turbulence. Basically, these studies are an improvement of the analytic studies discussed above. The other type models the macroscopic evolution of the density layer (length scales $0.1 \lesssim kL_n \lesssim 3$). These simulations have generally been performed in configuration space using finite-difference techniques [Zalesak and Ossakow, 1980; Zalesak et al., 1985; Mitchell et al., 1985] although there have recent simulations using pseudo-spectral techniques [Zargham and Seyler, 1987; Kelley et al., 1987]. We now discuss in detail the important results from these types of simulations.

(1) Small-Scale Structure. We first discuss simulation studies of small-scale turbulence, i.e., $kL_n >> 1$. We study the steady state turbulence that develops in a model system described as follows. A weakly collisional, magnetized plasma ($\mathbf{B} = B_0\,\mathbf{e}_z$) is confined between two horizontal conducting boundaries a distance L apart; the plasma density at the upper boundary (x = L) is higher than that at the lower boundary (x = 0). An ambient electric is in the y-direction, $\mathbf{E} = E_0\,\mathbf{e}_y$. Thus, the system

is unstable to the $\underset{\sim}{E} \times \underset{\sim}{B}$ instability. This model is clearly not a complete representation of the ionospheric plasma; its chief advantages are that it is a well-posed problem and it admits steady state solutions (see Rognlien and Weinstock (1974)).

The coupled equations for the perturbed density and potential are given by (29) and (30). These equations are solved using a pseudo-spectral method code developed by Fyfe et al. (1977) and is based on the work of Orszag (1971). The dependent variables $\tilde{n}$ and $\tilde{\phi}$ are Fourier-decomposed as follows:

$$\tilde{n}(\underset{\sim}{x},t) = \sum_{\underset{\sim}{k}} \tilde{n}(\underset{\sim}{k},t)\exp(i\underset{\sim}{k}\cdot\underset{\sim}{x}) \tag{47a}$$

$$\tilde{\phi}(\underset{\sim}{x},t) = \sum_{\underset{\sim}{k}} \tilde{\phi}(\underset{\sim}{k},t)\exp(i\underset{\sim}{k}\cdot\underset{\sim}{x}) \tag{47b}$$

where $\underset{\sim}{k} = k_x \hat{e}_x + k_y \hat{e}_y$ and k_x and k_y are integers. The nonlinear $\underset{\sim}{E} \times \underset{\sim}{B}$ term (RHS of (29)) is computed by fast Fourier transforming $\nabla\tilde{n}$ and $\nabla\tilde{\phi}$ from k space to x space, calculating the nonlinear term in x space by a simple multiplication, and then fast Fourier transforming the result back to k space. The equations are stepped forward in time in k space, and the cycle is repeated. Because of the imposition of conducting boundaries at $x = 0$ and $x = L$, we require that $v_x = 0$ at these boundaries (the plasma cannot flow through the boundaries). This leads to the following conditions on $\tilde{n}$ and $\tilde{\phi}$: $\tilde{n}(k_x,k_y) = -\tilde{n}^*(k_x,k_y)$ and $\tilde{\phi}(k_x,k_y) = -\tilde{\phi}^*(k_x,k_y)$.

We present some representative results of this type of simulation study in Figs. 8 and 9. These results are from the paper by Hassam et al. (1986) in which the nonlinear evolution on the Rayleigh-Taylor instability was investigated. We mention that (29) and (30) are equivalent to the equations used in Hassam et al. (1986) if we make the identification that $V_0 = g/\Omega_i\nu_{in}$. The numerical results are computed on a 32×32 mesh; in order to prevent aliasing of the wave energy during the fast Fourier transformation, all modes with $|\underset{\sim}{k}| > 32/3$ are set to zero amplitude. The plasma was initialized with small amplitude, randomly distributed modes. Two stages were clearly discernible in the temporal evolution of the system: (1) the linear stage in which the $\underset{\sim}{k}$ spectrum develops peaks at small k_x and large k_y in accordance with linear theory (see (27)), and (2) the nonlinear stage in which the system reaches a turbulent state with a broad spectrum of modes.

In Fig. 8 we plot the total energy in the system as a function of time where the energy is defined as

$$E = \frac{1}{2} \sum_{\underset{\sim}{k}} k^2 |\phi_{\underset{\sim}{k}}|^2 \tag{48}$$

Initially there is a slight decrease in energy because many of the modes are damped. However, this is followed by the linear phase in which the unstable modes grow exponentially up until $t \sim 50$. Following this the plasma modes are strongly nonlinear and the instability saturates; the total energy is roughly constant for $t > 100$.

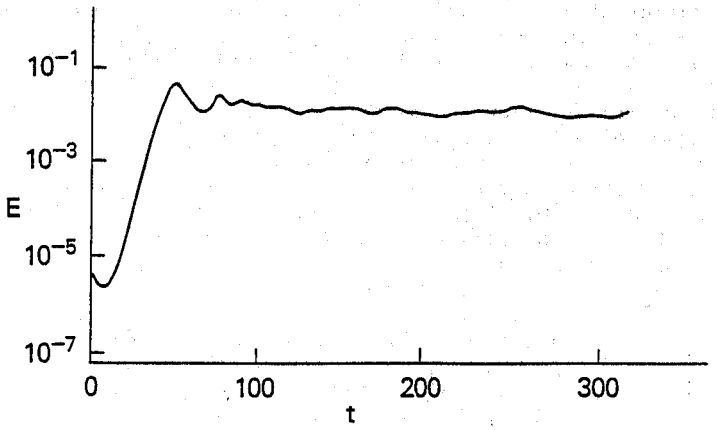

Fig. 8) Plot of total wave energy (E) vs time (t) during the evolution of the $\underset{\sim}{E} \times \underset{\sim}{B}$ instability (from Hassam et al. (1986)).

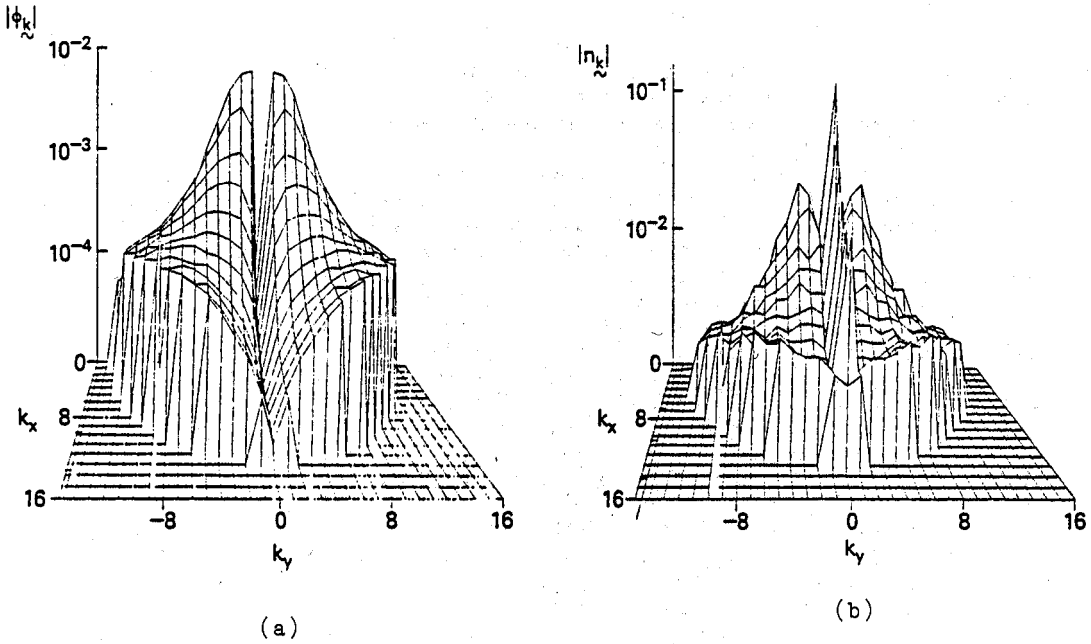

Fig. 9) Plot of the two dimensional, time averaged mode structure of the electrostatic potential and density fluctuations for the $\underset{\sim}{E} \times \underset{\sim}{B}$ instability (from Hassam et al. (1986)).

After the total energy saturates, the amplitudes of the wave modes can still be dynamic as energy is exchanged between different modes. The general characteristics of the spectra, however, remain unchanged: most of the energy resides in the longer wavelengths, and a power law type of falloff to shorter wavelengths is found. In order to see these features we present show Fig. 9 in which the time-averaged potential and density fluctuation spectra are shown in $\underset{\sim}{k}$ space. Note that the spectra have been reasonably smoothed out by the averaging process. Clearly, the bulk of the power resides in the long wavelength modes, small k_x and k_y. Interestingly, the potential spectrum is very anisotropic with relatively little energy in the region around $k_y \sim 0$. This is consistent with (30) in which the RHS is zero for $k_y = 0$. On the other hand, the density spectrum shows a peak in amplitude around the region $k_y \sim 0$. This is a reflection of the fact that while on average the turbulence tends to flatten the background density profile (i.e., $k_y = 0$), the fact that we hold the density fixed at $x = 0$ and $x = L$ results in sharp gradients near the boundaries leading to a substantial amount of power in the $k_y \sim 0$ density fluctuations.

Finally, we present the time-averaged power spectra (P_x and P_y) of the potential in Fig. 10. Here, P_x and P_y are defined as

$$P_x(k_x) = \sum_{k_y} |\phi_{\underset{\sim}{k}}|^2 \tag{49a}$$

$$P_y(k_y) = \sum_{k_x} |\phi_{\underset{\sim}{k}}|^2 \tag{49b}$$

The approximate spectral indices, obtained by a least squares fit, are also shown in Fig. 10. We note that there is a definite anisotropy as indicated by the difference in the slopes of P_x and P_y; specifically, we find that $P_x \propto k_x^{-3.7\pm0.3}$ and $P_y \propto k_y^{-4.6\pm0.3}$.

Finally, we comment that the above discussion has not focussed on the quantitative details of the simulations. The purpose of this section is to give the reader a general understanding of the nonlinear, many-mode coupling process, an example of one simulation method used to study this process, and examples of the type of insights that can be gained from this study (e.g., wave spectra, spectral indices). We note that this type of analysis can also be carried using finite difference simulation codes and we refer the interested reader to Keskinen and Ossakow (1983).

(2) Large-Scale Structure. We now discuss nonlinear simulations of the $\underset{\sim}{E} \times \underset{\sim}{B}$ instability relevant to the regime $kL_n \sim O(1)$. A number of simulations in this regime has been carried out at the Naval Research Laboratory over the past decade [Zalesak and Ossakow, 1980; Keskinen and Ossakow, 1982; Zalesak et al., 1985; Mitchell et al., 1985; Huba et al., 1988a,b]. The first point we wish to stress is that the full nonlinear equations are solved numerically. That is, the dependent variables (density and potential) are solved exactly; they are not split into equilibrium and perturbation quantities. Thus, there is no need to impose the condition that fluctuating quantities remain small as in the previous section. Moreover, the ambient density profile can evolve dynamically and self-consistently with the changes in the electrostatic potential. For simplicity, we show results from a simulation in the collisional regime ($\nu_{in} \gg \omega$). This corresponds to the situation where the density and potential perturbations are confined to the F region, i.e., there is no coupling to the magnetosphere. We discuss a magnetosphere-ionosphere coupling model of

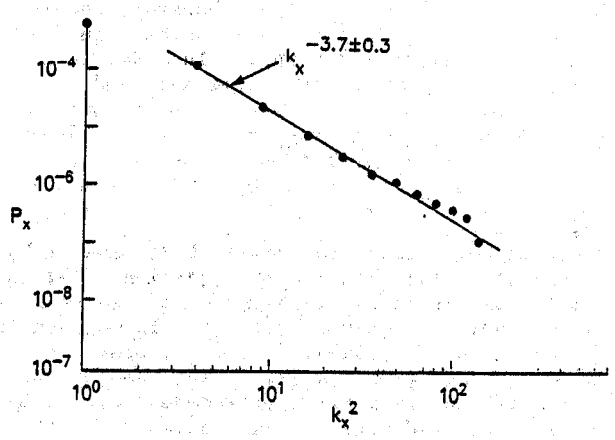

Fig. 10) Plot of the power spectral density [P_x and P_y] associated with the electrostatic potential ϕ (from Hassam et al. (1986)).

plasma instabilities in the Appendix. The equations being solved are continuity and current conservation:

$$\frac{\partial n}{\partial t} + \nabla \cdot n\underset{\sim}{V}_e = 0 \tag{50}$$

$$\nabla \cdot n\nabla\phi = 0 \tag{51}$$

where $\underset{\sim}{V}_e = -c\nabla\phi/B \times \hat{e}_z$.

The numerical methods used to solve (49) and (50) are described in Zalesak et al. (1985). The continuity equation (49) is solved using the multi-dimensional flux-corrected techniques of Zalesak (1979) while the potential equation (50) is solved with the incomplete Cholesky conjugate gradient algorithm of Hain (1980). The simulations presented here are performed on a 100 x 80 grid (x,y). The ambient density is initially characterized by a 1.5 to 1.0 density enhancement with a Gaussian profile of scale size 6 km in the x-direction and uniform in the y-direction. The ambient magnetic field is in the z-direction (B_0 = 0.5 G), and an ambient electric field is in the y-direction (E_0 = 0.025 V/m). The entire density enhancement $\underset{\sim}{E} \times \underset{\sim}{B}$ drifts in the x-direction with a velocity V_x = 500 m/sec. Periodic boundary conditions are assumed in the y-direction, and the grid is initialized with a random 1% density fluctuation.

The results of the simulation in shown in Fig. 11. The behavior of the density profile is typical of that observed in previous simulations [Keskinen and Ossakow, 1983]. In panel 2 (t = 520 sec) we see that a set of "fingers" has begun to form. The high density fingers grow outward into the low density background, while the low density fingers penetrate into the high density region. Subsequent nonlinear evolution involves the continued elongation of these fingers in the x-direction, with very little apparent change in their size in the y-direction. The original density enhancement is ultimately sliced into a group of sheets parallel to the initial density gradient.

Although Fig. 11 clearly shows the development of plasma structure in the plane transverse to B, one cannot directly compare Fig. 11 with any satellite or rocket data which is only one dimensional. Thus, in order to facilitate the comparison between the observational data and the simulation results, we plot density versus distance in Fig. 12 for three different satellite paths. We define θ to be the angle between the satellite path ($\underset{\sim}{x}_S$) and the -x-direction, i.e., $\theta = \cos^{-1}(-\underset{\sim}{x}_S \cdot \underset{\sim}{e}_x/|\underset{\sim}{x}_S|)$ (see Fig. 11). The striking features of Fig. 12 are the following. First, the perceived scale size of the ambient density profile varies considerably for the different paths. The actual scale size is roughly 6 km which is evident in the top panel (θ = 0°). However, for paths that slice the gradient at an angle one may be "fooled" into thinking that the scale size of the density profile is much larger than 6 km. Second, the density fluctuations look very different depending on the path. The top panel (θ = 0°) suggests that the density isn't very structured because the path only intersects one striation (or elongation). However, for paths which cut across many striations, as in the bottom two panels (θ = 63° and 83°), the density looks highly structured. Also, for the case θ = 83°, there is a considerable amount of plasma structure for x > 40 km, a region where there is no apparent background density gradient which could drive the instability. This is primarily a reflection of the fact that the instability has proceeded far enough to effectively destroy the original plasma structure.

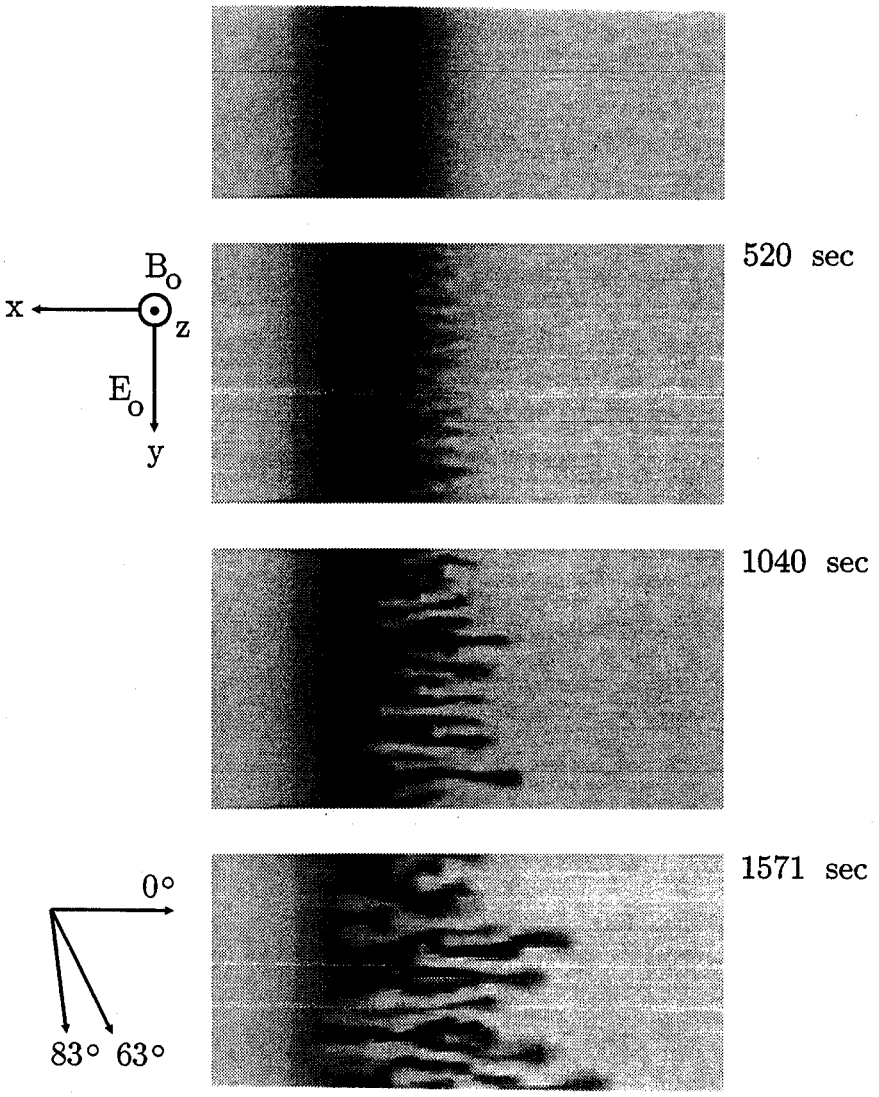

Fig. 11) Temporal evolution of the collisional $\vec{E}$ x $\vec{B}$ instability as it structures a Gaussian density enhancement.

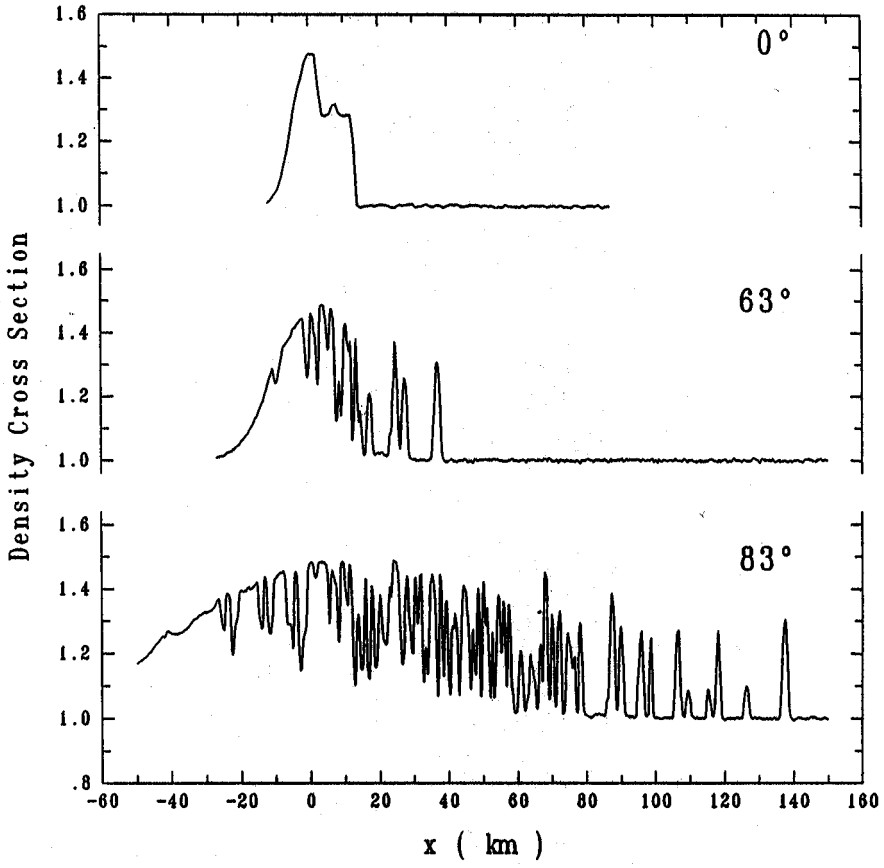

Fig. 12) Plot of the density (n) vs distance (x_s) where the path corresponds to a satellite moving at angle θ relative to the x-direction [(a) θ = 0°, (b) θ = 63°, (c) θ = 83°]. It is important to note how different the structure looks depending on the path.

Given this background, we now discuss experimental observations which support the contention that $\mathbf{E} \times \mathbf{B}$ instability is the source of high latitude turbulence (at times).

V. EXPERIMENTAL OBSERVATIONS

As noted by Tsunoda (1989) the most convincing evidence that the $\mathbf{E} \times \mathbf{B}$ instability is active in the high latitude ionosphere is reported by Cerisier et al. (1985) based on data from the Aureol 3 satellite. In this paper, electric field and density fluctuations, with reported scale sizes of 100's m to a few km, are found to occur asymmetrically on larger scale density enhancements (sizes of the order of 10's km). That is, on one side of the density enhancement plasma turbulence is observed, while on the other side the density profile is smooth. This is shown very clearly in Fig. 13 which is from Tsunoda (1989). Note in the top panel that the left hand sides of the density enhancements are structured, while the right hand sides, although much steeper, are unstructured. This is consistent with the necessary condition for the onset of the $\mathbf{E} \times \mathbf{B}$ instability which requires that $\mathbf{E}_0 \times \mathbf{e}_z \cdot \nabla n_0 > 0$. Cerisier et al. (1985) found that this condition was satisfied for more than half of the observations of the type shown in Fig. 13 (i.e., 4 out of 6). However, it should also be pointed out that it is very difficult for a single satellite to unambiguously determine whether or not this criterion is satisfied. This is because only the component of the density gradient along the path of the satellite is known. The real gradient (i.e., shortest density gradient scale length) can have any direction within 90° of the observed one.

To illustrate the difficulties of interpreting data from only a single satellite, we plot the density profiles based on our simulation results (shown in Fig. 12) as a function of time instead of space. That is, we will assume that a spacecraft passes through the plasma structure observed in the simulations at a velocity of ~ 7 km/sec. The results are shown in Fig. 14. Note that when θ is large, the "perceived" gradient scale length can be considerably larger than the actual scale length of 6 km. By the same token, the perceived scale size of the plasma structure also varies depending on the path as noted on Fig. 14. Thus, although it is difficult to make a definitive, quantitative comparison between observational data and simulation results, the evidence for the occurrence of the $\mathbf{E} \times \mathbf{B}$ instability in the high latitude ionosphere is very compelling.

VI. SUMMARY

We have presented a general overview of the theoretical and computational methods used to study plasma instabilities in the high latitude ionosphere. We illustrated the various methods with the $\mathbf{E} \times \mathbf{B}$ instability being the "guinea pig". The fundamental concepts and techniques are rather general and can be applied to other instabilities. Aside from going through several types of analytical and numerical calculations, we also tried to emphasize the physical conditions for which the different methods are valid, and the limitations of each method. It is also important to mention that, for pedagogical purposes, we have considered only the simplest model possible to describe the $\mathbf{E} \times \mathbf{B}$ instability in the high latitude ionosphere. There are a host of other physical processes which have been neglected, but should be included in a self-consistent manner. One major issue involves the coupling of the wave fields to the E-region and the magnetosphere, and understanding how the coupling impacts the evolution of the instability. Preliminary calculations suggest that coupling can

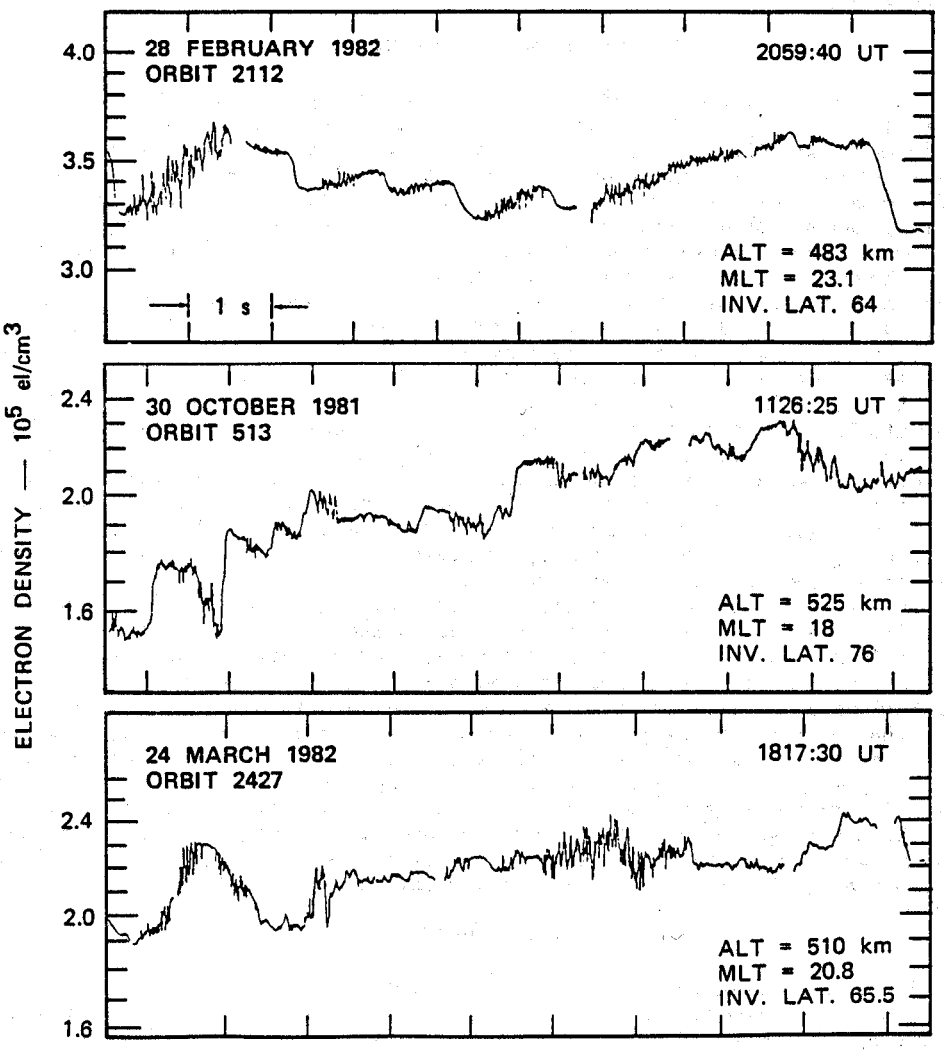

Fig. 13) Plot of density (n) vs time (t) from Aureol 3 satellite data (from Tsunoda (1989)).

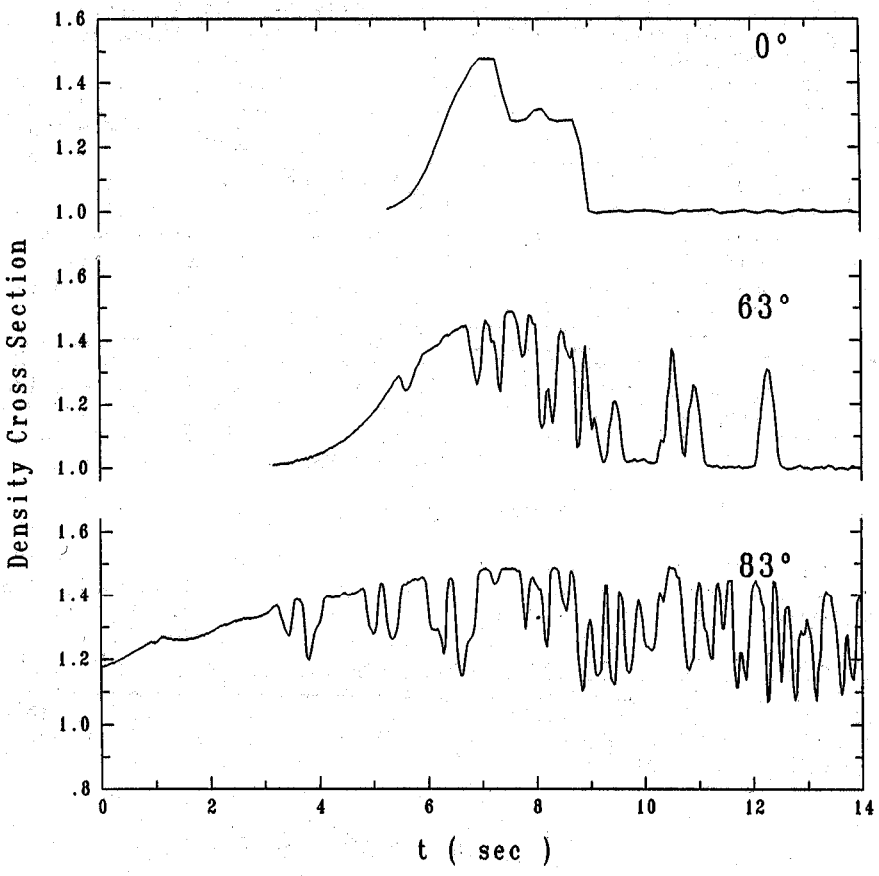

Fig. 14) Plot of density (n) vs time (t) based on the data in Fig. 12. We transform to from space to time assuming an orbital velocity V = 7 km/sec.

dramatically affect structure evolution and are discussed in the Appendix [Mitchell et al., 1985].

Closely related to the coupling issue is the issue of three dimensional dynamics, i.e., relaxing the equipotential field line approximation. This is a difficult problem and extremely pertinent to virtually all high latitude physical processes. Some research has been done regarding the linear theory of the $\mathbf{E} \times \mathbf{B}$ instability including parallel dynamics [Sperling et al., 1984; Drake et al., 1985; Huba and Chaturvedi, 1987]. Recently, there has been the successful development of a 3D electrostatic code to describe the evolution of ionospheric barium clouds which can be applied to high latitude processes [Drake et al., 1988; Zalesak et al., 1988].

Finally, it should be noted that the subject of high latitude ionospheric turbulence is very complex and not completely understood at this time. Although the $\mathbf{E} \times \mathbf{B}$ instability appears to be successful in explaining some observations in the sub-kilometer range, it certainly cannot explain all of them. In particular, some recent observations [Kintner, 1976; Basu et al., 1986; Basu et al., 1988] suggest that velocity shears are playing a role in the development of plasma structure. These observations have spurred interest in how velocity shear impacts the $\mathbf{E} \times \mathbf{B}$ instability [Huba et al., 1983], and in the Kelvin-Helmholtz instability [Kintner and Seyler, 1985; Keskinen et al., 1988] and other velocity shear instabilities [Ganguli and Palmadesso, 1988; Ganguli et al., 1988; Basu and Coppi, 1988].

ACKNOWLEDGMENTS

Discussions with my colleagues at the Naval Research Laboratory (M.J. Keskinen, J.A. Fedder, S.L. Ossakow, S.T. Zalesak, P.K. Chaturvedi) and Science Applications International Corporation (P. Satyanarayana, H.G. Mitchell, A.B. Hassam, J.F. Drake) over the past decade have been an enormous help to me in understanding instability processes in the ionosphere (and elsewhere), and are gratefully acknowledged. I especially thank H.G. Mitchell for providing the graphics and data analysis associated with the simulations discussed in Section IV.B.2 and the Appendix. This work has been supported by ONR and DNA.

APPENDIX: MAGNETOSPHERE-IONOSPHERE COUPLING MODEL

A relatively simple model of the effect of magnetosphere-ionosphere coupling on high latitude instabilities has been developed at NRL [Mitchell et al., 1985; Keskinen et al., 1988]. We have described this model in the first WITS Handbook [Huba et al., 1988b]. We include another discussion of the subject here for the sake of completeness, and to relate the theoretical analysis of Section III to this model.

We first discuss some underlying concepts associated with ionosphere-magnetosphere coupling and the evolution of plasma instabilities. The $\underline{E} \times \underline{B}$ instability is primarily an electrostatic flute mode; that is, it generates perturbations in the density and/or electric field transverse to the magnetic field $\underline{B}$ rather than parallel to $\underline{B}$. Moreover, the magnetic field remains constant, i.e., unperturbed. Alternatively, one can say that the perturbed transverse electric fields map perfectly along $\underline{B}$ (i.e., the magnetic field lines are equipotential lines). [Strictly speaking, it is expected that (1) the magnetic field lines are not perfect equipotential lines and (2) the magnetic field will be disturbed by any instability.] We note the following. First, the transverse electric field will have an e-folding distance along the magnetic field given by $L_{||} \simeq k_{\perp}^{-1} (\sigma_{||}/\sigma_{\perp})^{1/2}$ where $k_{\perp}$ is the transverse wave number of the electric field perturbation and $\sigma_{||(\perp)}$ is the parallel (perpendicular) conductivity [Farley, 1959]. For the high latitude F region we note that $\sigma_{||}/\sigma_{\perp} \gtrsim 10^6$; thus, kilometer scale irregularities can map well into the magnetosphere. Second, the disturbance will propagate along the magnetic field at the Alfvén velocity. The parallel distance it will travel is given by $L_A \simeq V_A/\gamma$ where γ is the characteristic growth rate of the instability and V_A is the Alfvén velocity. For the high latitude F region we note that $\gamma \lesssim 0.1$ sec and $V_A \gtrsim 10^3$ km/sec so that $L_A \gtrsim 10^4$ km. Again, on the time scale of the instability, the modes can map well into the magnetosphere. Conversely, modes generated in the magnetosphere can couple to the ionosphere.

Given this background we now describe our model. To simplify the analysis we will assume the modes are electrostatic. This means that the time scales of interest in the problem are long compared to the transit time of an Alfvén wave across the modeled region along the magnetic field. This assumption implies that the plasma is quasi-neutral everywhere, and that the electric field perpendicular to the magnetic field maps perfectly along the field within the modeled region. Further, since the electrons have a greater mobility parallel to the magnetic field than the ions, we assume that parallel currents are electron currents and that the ions have no velocity parallel to the field. As a result of these assumptions, the model may be viewed as a set of ion layers perpendicular to the magnetic field which are strongly linked by the mapping of the perpendicular electric field between layers and by the parallel electron currents which flow between layers in order to preserve quasi-neutrality. This is shown in Fig. 15.

For each layer, the governing equations are the continuity and momentum equations for each species, i.e., (1) and (2). In order to maintain quasi-neutrality (i.e., $\nabla \cdot \underline{J} = 0$) it is assumed that all currents generated within this model must also close within this model. The field-line integrated divergence of the perpendicular current must therefore be zero, i.e.,

$$0 = \int dz\ \nabla_\perp \cdot \underset{\sim}{j}_\perp = \nabla_\perp \cdot \left(\underset{\sim}{J}_{\perp Ped} + \underset{\sim}{J}_{\perp pol}\right)$$

$$= \nabla \cdot \left(\Sigma_p\left[-\nabla_\perp\phi\right] - C_M\left[\frac{\partial}{\partial t} + \frac{c}{B}\left(\hat{e}_z \times \nabla_\perp\phi\right) \cdot \nabla\right]\nabla_\perp\phi\right) \qquad \text{(A1)}$$

where $\underset{\sim}{J}_{\perp Ped}$ and $\underset{\sim}{J}_{\perp pol}$ are the field-line integrated Pedersen and polarization currents (see Fig. 15), $\Sigma_p = \int(nec\nu_i/B\Omega_i)dz$ is the field-line integrated Pedersen conductivity, and $C_M = \int(nec/B\Omega_i)dz$ is the field-line integrated inertial capacitance. For details of this derivation see Mitchell et al. (1985). Thus, the plasma on each level E x B drifts under the influence of the perpendicular electric field ($\underset{\sim}{E} = -\nabla\phi$), which is itself determined by the fact that the perpendicular Pedersen and polarization drift currents driven by the field must close by means of parallel electron currents within the model.

The Pedersen currents tend to decay any potential which is not supported by the density gradients, while the polarization drift currents tend to slow this decay. As a result, the balance between these effects defines an inertial relaxation rate $\nu = \Sigma_p/C_M$ for changes in the potential. The relative importance of Pedersen versus polarization currents is dictated by the parameter ν/γ where γ is the linear growth rate of the instability under investigation. Pedersen currents dominate when $\nu/\gamma >> 1$ and polarization currents dominate when $\nu/\gamma << 1$. Thus, ion inertia is playing a significant role in the evolution of the instability when magnetospheric coupling is important; this is the reason we included ion inertia in the theoretical analysis in this paper.

To demonstrate the effect of magnetosphere-ionosphere coupling on the evolution of the $\underset{\sim}{E}$ x $\underset{\sim}{B}$ gradient drift instability we present the results of a simulation in which magnetospheric coupling is dominant. These results should be contrasted to those shown in Fig. 11 in which magnetospheric coupling is ignored. The physical configuration is the same as that described for Fig. 11. We only consider structure in the plane transverse to the ambient magnetic field, i.e., the xy plane. The F-layer is initially characterized by a 1.5 to 1.0 density enhancement with a Gaussian profile of scale size 12 km in the x-direction and uniform in the y-direction, a uniform magnetic field in the z-direction (B_z = 0.5 G), and a background electric field in the y-direction (E_y = .025 V/m). The entire enhancement E x B drifts in the x-direction at a velocity v_x = 0.5 km/sec. Finally, we consider ν/γ = 0.20 so that the polarization current dominates over the Pedersen current. A uniform horizontal magnetosphere is assumed above the F-layer linked by the vertical magnetic field lines. The back edge of the F-layer enhancement, relative to the drift, is unstable to the $\underset{\sim}{E}$ x $\underset{\sim}{B}$ gradient drift instability. The simulations are performed on an 100 x 80 cell grid (x,y) with a cell size of 1.0 km x .25 km which is drifting with the enhancement at the E_y x B velocity. Periodic boundary conditions are assumed in the y-direction, and the grid is initialized with a random 1% density fluctuation.

The evolution of structure in the inertial regime (i.e., strong ionosphere-magnetosphere coupling) is shown in Fig. 16, and is very different from the collisional case (see Fig. 11). The linear growth rate for this case is $\gamma \simeq 5.0 \times 10^{-3}$ sec^{-1} (or a growth time of $\tau \simeq 200$ sec) so that the growth of the mode is retarded by ionosphere-magnetosphere coupling. During the time period between panel 1 and panel 2 ($t < 704$ sec), the growth of the instability closely resembles that of Fig. 11. There is development of long, narrow density fingers. However, for $t > 700$ seconds,

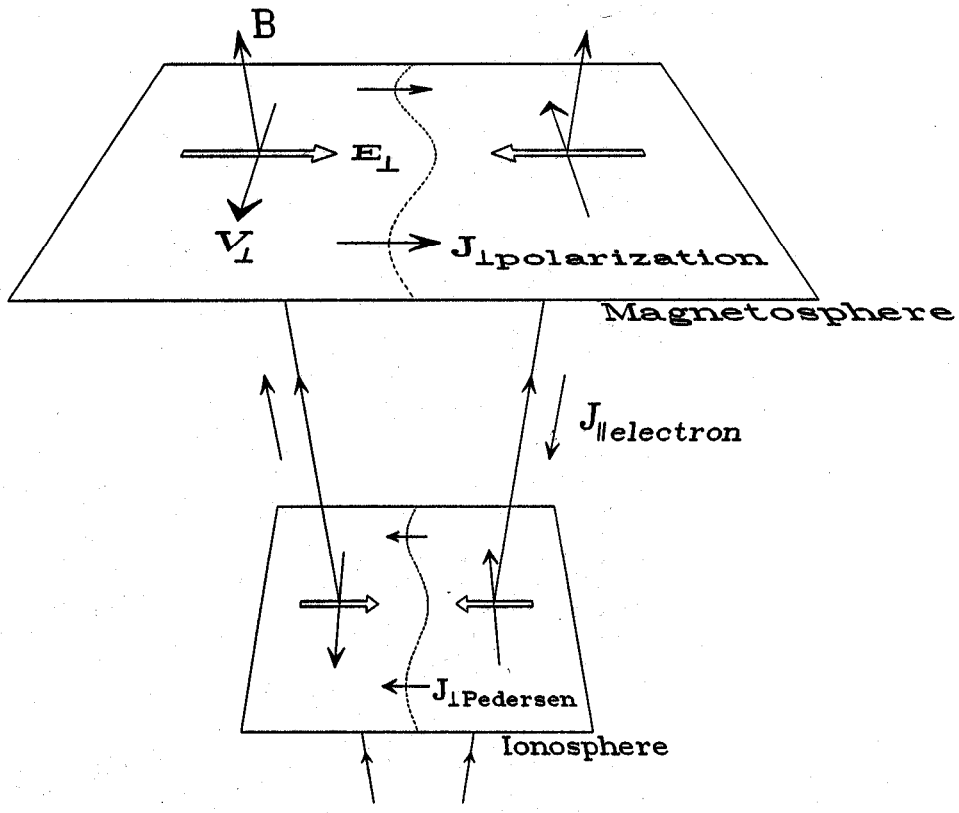

Fig. 15) Schematic of the physical model used for magnetospheric-ionospheric coupling. The coupling between the ionosphere and the magnetosphere is maintained by parallel electron currents flowing along equipotential field lines. The perpendicular currents are the Pedersen current in the ionosphere, and the polarization current in the magnetosphere.

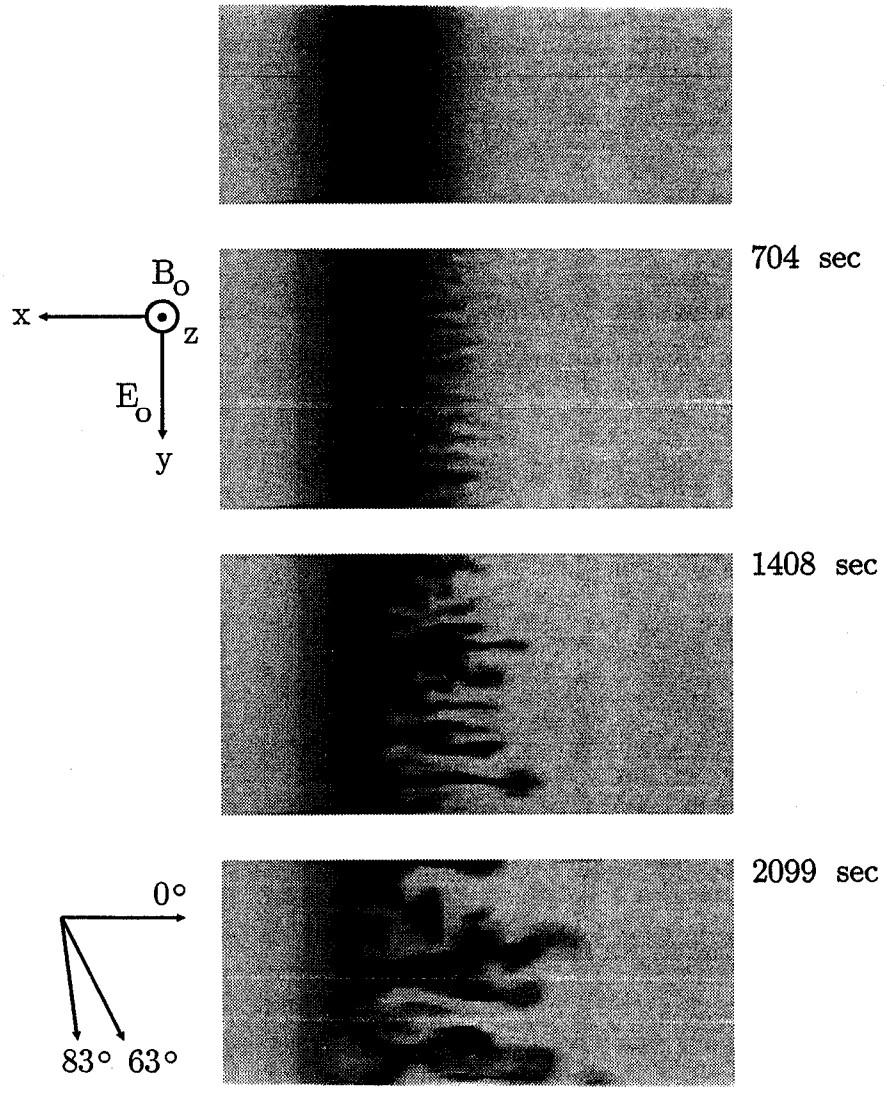

Fig. 16) Temporal evolution of the inertial $\underline{E}$ x $\underline{B}$ instability as it structures a Gaussian density enhancement. In this situation the magnetosphere is playing an important role in the structuring process.

the behavior changes radically from that in Fig. 11. In panels 3 and 4, we see that the fingers form mushroom-like heads and tend to thicken. No longer are they long, thin interpenetrating fingers; rather they are fat interpenetrating blobs. Any narrow fingers which begin to form quickly go to a mushroom shape and then spread out. In a number of simulations we have noted a tendency for the structure in the y direction to undergo an inverse cascade to the longest mode which will fit in the system. This feature can clearly be seen in panel 4, where the structured state throughout most of the simulation region shows two blobs: one of high density, and the other of low density.

REFERENCES

Baker, K.B., R.A. Greenwald, and R.T. Tsunoda, Very high latitude F-region irregularities observed by HF-radar backscatter, Geophys. Res. Lett., 10, 904, 1983.

Basu, B. and B. Coppi, Fluctuations associated with sheared velocity regions near auroral arcs, Geophys. Res. Lett., 15, 417, 1988.

Basu, Su, S. Basu, C. Senior, D. Weimer, E. Nielsen, and P.F. Fougere, Velocity shears and sub-km scale irregularities in the nighttime auroral F-region, Geophys. Res. Lett., 13, 101, 1986.

Basu, Su., S. Basu, E. MacKenzie, P.F. Fougere, W.R. Coley, N.C. Maynard, J.D. Winningham, M. Sugiura, W.B. Hanson, and W.R. Hoegy, Simultaneous density and electric field fluctuation spectra associated with velocity shears in the auroral oval, J. Geophys. Res., 93, 115-136, 1988.

Cerisier, J.C., J.J. Berthelier, and C. Beghin, Unstable density gradients in the high latitude ionosphere, Radio Sci., 20, 755, 1985.

Chandrasekhar, S., Hydrodynamic and Hydromagnetic Stability, (Clarendon, Oxford, 1961).

Chaturvedi, P.K., and S.L. Ossakow, Nonlinear theory of the collisional Rayleigh-Taylor instability in equatorial Spread F, Geophys. Res. Lett., 4, 558, 1977.

Chaturvedi, P.K., and S.L. Ossakow, Nonlinear stabilization of the $\underline{E} \times \underline{B}$ gradient drift instability in ionospheric plasma clouds, J. Geophys. Res., 84, 419, 1979.

Chaturvedi, P.K., and S.L. Ossakow, The current convective instability as applied to the auroral ionosphere, J. Geophys. Res., 86, 4811, 1981.

Chaturvedi, P.K. and J.D. Huba, The interchange instability in high latitude plasma blobs, J. Geophys. Res., 92, 3357, 1987.

Drake, J.F., J.D. Huba, and S.T. Zalesak, Finite temperature stabilization of the gradient drift instability in barium clouds, J. Geophys. Res., 90, 5227, 1985.

Drake, J.F., M. Mulbrandon, and J.D. Huba, Three-dimensional equilibrium and stability of ionospheric plasma clouds, Phys. Fluids, 31, 3412, 1988.

Farley, D.T., A theory of electrostatic fields in a horizontally stratified ionosphere subject to a vertical magnetic field, J. Geophys. Res., 64, 1225, 1959.

Fyfe, D., G. Joyce, and D. Montgomery, Magnetic dynamo action in two-dimensional turbulent magnetohydrodynamics, J. Plasma Phys., 17, 317, 1977.

Ganguli, G. and P.J. Palmadesso, Electrostatic ion instabilities in the presence of parallel currents and transverse electric fields, Geophys. Res. Lett., 15, 103, 1988.

Ganguli, G., Y.C. Lee, and P.J. Palmadesso, Kinetic theory for electrostatic waves due to transverse velocity shears, Phys. Fluids, 31, 823, 1988.

Gary, S.P. and M. Thomsen, Collisionless electrostatic interchange instabilities, J. Plasma Phys., 28, 551, 1982.

Gary, S.P. and T.E. Cole, Pedersen density drift instabilities, J. Geophys. Res., 88, 10104, 1983.

Hain, K., A non-recursive incomplete Cholesky decomposition method for the solution of linear equations with a sparse matrix, NRL Memorandum 4264, Naval Research Laboratory, Washington, DC, (1980).

Hassam, A.B., W. Hall, J.D. Huba, and M.J. Keskinen, Spectral characteristics of interchange turbulence, J. Geophys. Res., 91, 13513, 1986.

Huba, J.D. and S.T. Zalesak, Long-wavelength limit of the $\underline{E} \times \underline{B}$ instability, J. Geophys. Res., 88, 10263, 1983.

Huba, J.D., S.L. Ossakow, P. Satyanarayana, and P.N. Guzdar, Linear theory of the $\underline{E} \times \underline{B}$ instability with an inhomogeneous electric field, J. Geophys. Res., 88, 425, 1983.

Huba, J.D., A.B. Hassam, I.B. Schwartz, and M.J. Keskinen, Ionospheric turbulence: Interchange instabilities and chaotic fluid behavior, Geophys. Res. Lett., 12, 65, 1985.

Huba, J.D., H.G. Mitchell, M.J. Keskinen, J.A. Fedder, P. Satyanarayana, and S.T. Zalesak, Simulations of plasma structure evolution in the high-latitude ionosphere, Radio Sci., 23, 503, 1988a.

Huba, J.D., H.G. Mitchell, M.J. Keskinen, J.A. Fedder, P. Satyanarayana, and S.T. Zalesak, Simulations of plasma structure evolution in the high-latitude ionosphere, WITS Handbook Vol. 1, ed. C.H. Liu and B. Edwards, 140, 1988b.

Huba, J.D., Theoretical and simulation methods applied to high latitude ionospheric turbulence, to appear in Proc. of MIT Space Sci. Sym., ed. T. Chang, 1989.

Huba, J.D., G. Ganguli, P. Satyanarayana, A.B. Hassam, and D. Winske, Generalized interchange instability in a finite β, collisional plasma, to be submitted to Phys. Fluids, 1989.

Kelley, M.C., J.F. Vickrey, C.W. Carlson, and R. Torbert, On the origin and spatial extent of high-latitude F region irregularities, J. Geophys. Res., 87, 4469, 1982.

Kelley, M.C., C.E. Seyler, and S. Zargham, Collisional interchange instability, 2, A comparison of the numerical simulations with the in situ experimental data, J. Geophys. Res., 92, 10089, 1987.

Keskinen, M.J. and S.L. Ossakow, On the spatial power spectrum of the $\underline{E} \times \underline{B}$ gradient drift instability in ionospheric plasma clouds, J. Geophys. Res., 86, 6947, 1981.

Keskinen, M.J. and S.L. Ossakow, Nonlinear evolution of plasma enhancements in the auroral ionosphere, 1, Long wavelength irregularities, J. Geophys. Res., 89, 144, 1982.

Keskinen, M.J. and S.L. Ossakow, Nonlinear evolution of convecting plasma enhancements in the auroral ionosphere, 2, Small scale irregularities, J. Geophys. Res., 88, 474, 1983.

Keskinen, M.J. and S.L. Ossakow, Theories of high-latitude ionospheric irregularities: a review, Radio Sci., 18, 1077, 1983.

Keskinen, M.J., H.G. Mitchell, J.A. Fedder, P. Satyanarayana, S.T. Zalesak, and J.D. Huba, Nonlinear evolution of the Kelvin-Helmholtz instability in the high-latitude ionosphere, J. Geophys. Res., 93, 137, 1988.

Keskinen, M.J., Scaling laws for the spectrum of interchange instabilities in the high latitude ionosphere, to be submitted to J. Geophys. Res., 1989.

Kintner, P.M., Observations of velocity shear driven plasma turbulence, J. Geophys. Res., 81, 5114, 1976.

Kintner, P.M. and C.E. Seyler, The status of observations and theory of high latitude ionospheric and magnetospheric plasma turbulence, Space Sci. Rev., 41, 91, 1985.

Krall, N.A. and A.W. Trivelpiece, Principles of Plasma Physics, (McGraw-Hill, New York, 1973).

Lorenz, E.N., Deterministic nonperiodic flow, J. Atmos. Sci., 20, 130, 1963.

Mitchell, H.G., J.A. Fedder, M.J. Keskinen, and S.T. Zalesak, A simulation of high latitude F layer instabilities in the presence of magnetosphere-ionosphere coupling, Geophys. Res. Lett., 12, 283, 1985.

Orszag, S.A., Numerical simulation of incompressible flows within simple boundaries. 1. Galerkin (spectral) representations, Stud. Appl. Math., 50, 293, 1971.

Ossakow, S.L., P.K. Chaturvedi, and J.B. Workman, High-altitude of the gradient drift instability, J. Geophys. Res., 83, 2691, 1978.

Rino, C.L., R.C. Livingston, and S.J. Matthews, Evidence for sheet-like auroral ionospheric irregularities, Geophys. Res. Lett., 5, 1038, 1978.

Roberts, K. and J.B. Taylor, Magnetohydrodynamic equations for finite Larmor radius, Phys. Rev. Lett., 8, 197, 1962.

Rodriquez, P. and E. Szuszczewicz, High latitude irregularities in the lower F-region: intensity and scale size distribution, J. Geophys. Res., 89, 5575, 1984.

Rognlien, T.D. and J. Weinstock, Theory of the nonlinear spectrum of the gradient drift instability in the equatorial electrojet, J. Geophys. Res., 79, 4733, 1974.

Sperling, J.L. and A.J. Glassman, Short-circuiting, ion-viscous, and ion-inertial effects in striation "freezing", J. Geophys. Res., 90, 8707, 1985.

Sperling, J.L., J.F. Drake, S.T. Zalesak, and J.D. Huba, The role of finite parallel length on the stability of barium clouds, J. Geophys. Res., 89, 10913, 1984.

Tsunoda, R.T., High-latitude F-region irregularities: A review and synthesis, Rev. of Geophys. and Spa. Sci., 1989 (in press).

Vickrey, J.F., C.L. Rino, and T.A. Potemra, Chatanika/Triad observations of unstable ionization enhancements in the auroral F region, Geophys. Res. Lett., 7, 789, 1980.

Zalesak, S.T., Fully multidimensional flux-corrected transport algorithms for fluids, J. Comp. Phys., 31, 335, 1979.

Zalesak, S.T. and S.L. Ossakow, Nonlinear equatorial spread F: Spatially large bubbles resulting from large horizontal scale initial perturbations, J. Geophys. Res., 85, 2131, 1980.

Zalesak, S.T., P.K. Chaturvedi, S.L. Ossakow, and J.A. Fedder, Finite temperature effects on the evolution on ionospheric barium clouds in the presence of a conducting background ionosphere I. A high altitude incompressible background ionosphere, J. Geophys. Res., 90, 4299, 1985.

Zalesak, S.T., J.F. Drake, and J.D. Huba, Dynamics of three-dimensional ionospheric plasma clouds, Radio Sci., 23, 591, 1988.

Zargham, S. and C.E. Seyler, Collisional interchange instability, 1, Numerical simulations of intermediate-scale irregularities, J. Geophys. Res., 92, 10073, 1987.